Estimating Ground Motion Intensities Using Simulation-Based Estimates of Local Crustal Seismic Response

Himanshu Agrawal[1] and John McCloskey[1]†

[1]School of Geosciences, University of Edinburgh, Drummond Street Edinburgh, Edinburgh EH8 9XP, UK

†Deceased

Corresponding author: Himanshu Agrawal (himanshu.agrawal@ed.ac.uk), (himansh78@gmail.com)

Key Points:

- In the Global South, the absence of seismic catalogues impedes ground motion predictions that are crucial for earthquake-aware urban planning.
- Physics-based simulations can use hypothetical earthquakes to estimate ground motions without extensive earthquake data availability.
- The primary source of short-scale variability in ground motion is the local subsurface geology, making it a crucial focal point.

Abstract

It is estimated that 2 billion people will move to cities in the next 30 years, many of which possess high seismic risk, underscoring the importance of reliable hazard assessments. Current ground motion models for these assessments typically rely on an extensive catalogue of events to derive empirical Ground Motion Prediction Equations (GMPEs), which are often unavailable in developing countries. Considering the challenge, we choose an alternative method utilizing physics-based (PB) ground motion simulations, and develop a simplified decomposition of ground motion estimation by considering regional attenuation (Δ) and local site amplification (A), thereby exploring how much of the observed variability can be explained solely by wave propagation effects. We deterministically evaluate these parameters in a virtual city named Tomorrowville, located in a 3D layered crustal velocity model containing sedimentary basins, using randomly oriented extended sources. Using these physics-based empirical parameters (Δ and A), we evaluate the intensities, particularly Peak Ground Accelerations (PGA), of hypothetical future earthquakes. The results suggest that the estimation of PGA using the deterministic $\Delta - A$ decomposition exhibits a robust spatial correlation with the PGA obtained from simulations within Tomorrowville. This method exposes an order of magnitude spatial variability in PGA within Tomorrowville, primarily associated with the near surface geology and largely independent of the seismic source. In conclusion, advances in PB simulations and improved crustal structure determination offer the potential to overcome the limitations of earthquake data availability to some extent, enabling prompt evaluation of ground motion intensities.

Plain Language Summary

Numerous cities in earthquake-prone regions of the Global South are currently experiencing rapid growth, which poses a significant risk to their populations in the upcoming years. The attainment of effective urban planning, which takes earthquake vulnerabilities into account, typically needs access to long-term earthquake recordings for projecting ground shaking through to future seismic events. Regrettably, the scarcity of earthquake monitoring disproportionately hampers this potential in the Global South, resulting in the utilization of ground motion data from distant locations across the globe. This approach, however, comes with notable limitations

and contributes to the large uncertainty surrounding predictions of ground shaking. We approach this challenge by employing state-of-the-art physics-based simulation techniques that can use hypothetical earthquakes and numerically solve the seismic wave propagation through the Earth's crust. Our study shows that even when a comprehensive earthquake database is lacking, it is feasible to generate reasonably accurate predictions of the spatial variability in expected ground motions using high-resolution local geological information. We emphasize that in cases where urban planning choices need to be formulated for a city characterized by diverse geological features, substantial investments in the measurement of subsurface properties can prove valuable.

1 Introduction

(Baker et al., 2021; Bradley, 2019; Kramer, 1996; Kramer & Mitchell, 2006; Mcguire, 2008; Stirling, 2014; Stirling et al., 2012).The importance of robust ground motion modelling is particularly important during the current unprecedented global urbanization.The United Nations Human Settlements Programme (UN-Habitat) forecasts that by 2050 some 2 billion new citizens will move to urban centers so that, by then, some 68% of the world's population will live in cities (UN-Habitat, 2022). It is estimated that 95% of this urbanization will happen in the global south. Urban population growth is often accommodated by rapid urban expansion in areas with well-documented seismic risk. The problems of understanding and reducing disaster risk in such rapid development are significant, and while this expansion presents a major global challenge, it also provides a time-limited opportunity to provide evidence-based decision support for this new development (UNISDR, 2015). Efforts in earthquake risk reduction through urban planning guided by high-resolution- hazard assessmentground-motion modelling, could reduce disaster risk for hundreds of millions of these future citizens. This approach also provides a cost-efficient method by concentrating on new constructions, where the expenses related to implementing effective earthquake-resistant design and construction are significantly lower compared to the costs of retrofitting at a later stage.

Seismic hazard analysis informs building codes constraining construction of new development in earthquake prone areas through development of ground motion models (Baker et al., 2021; Bradley, 2019; Kramer, 1996; Kramer & Mitchell, 2006; Mcguire, 2008; Stirling, 2014; Stirling et al., 2012). Observed ~~Seismic hazard analysis informs building codes constraining construction of new development in earthquake prone areas. The~~ ground shaking is ~~hazard is~~a ~~a~~ result of the interaction between a range of individually heterogeneous fields and processes, leading to deep complexity in even the simplest relationships. ~~(Baker et al., 2021; Bradley, 2019; Kramer, 1996; Kramer & Mitchell, 2006; Mcguire, 2008; Stirling, 2014; Stirling et al., 2012).~~ Measures of ground shaking intensity, for example, show an expected systematic decrease with distance between the observation and source, but the systematics are overprinted by the interactions between the complexities of the event and the crustal volume explored by the seismic wave train. The result is high amplitude variability in the observed intensity. Note that the uncertainty in the observations, in either intensity or distance, makes only a small contribution to this variability; the variability is an intrinsic part of the process.

Consider a series of events recorded at large number of sensors. In the commonly applied approach, the analyst chooses a functional form for the systematic decay of intensity and uses some fitting procedure to estimate its parameters. The resulting model is commonly known as a Ground Motion Model (GMM) (Douglas & Aochi, 2008; Douglas & Edwards, 2016a, 2016b), and takes the form:

$$lnIM = \mu_{lnIM} + \sigma_{lnIM}.\epsilon \tag{1}$$

Where, IM is the required intensity measure, μ_{lnIM}, is the estimated mean-field intensity, σ_{lnIM}, is an estimate of the variability around the mean which is usually assumed to conform to a log-normal distribution and ϵ is the standard normal variate.

It is important to note that the μ_{lnIM} term does not just describe the attenuation of intensity with distance. Common forms of μ_{lnIM} attempt to parameterize descriptions of the physics of the entire process including source properties, such as focal mechanism and their resulting directivity, as well as the local response of the site using estimates of V_{s30} (time-averaged shear-wave velocity in the top 30m) and κ (high frequency attenuation parameter) for example (Aki, 1993; Borcherdt & Glassmoyer, 1992; Bradley, 2011; Hough & Anderson, 1988; Kaklamanos et al., 2013; Shi & Asimaki, 2017). Expressions for μ_{lnIM} in current GMMs include numerous parameters, use advanced statistical techniques to fit these complex functions, and represent a practical approach to a fundamentally intractable problem (Douglas & Edwards, 2016a).

In practice, an ergodic assumption is invoked in GMM development by aggregating the data from multiple spatial locations that is assumed to be equivalent to the distribution in time (Anderson & Brune, 1999). However, with the increasing data for a particular tectonic area, the non-ergodic or partial non-ergodic approaches are favoured which modify μ_{lnIM} and σ_{lnIM} based on calibration with the local data that is available (Bradley, 2015; Rodriguez-Marek et al., 2014; Stewart et al., 2017). It is observed that major component of ground motion amplification can be associated with the ~~the~~~~which can be attributed to~~ local geological factors e.g. sedimentary basins (Graves et al., 1998; Pilz et al., 2011; Zhu et al., 2018), surface topography (Lee et al., 2009; Maufroy et al., 2012; G. Wang et al., 2018), and soil conditions (Bazzurro & Cornell, 2004; Cramer, 2003; Torre et al., 2020). ~~site-specific effects (Bazzurro & Cornell, 2004a),~~ H~~h~~ence, the general practice in GMM development is dominated by using near-surface site-specific parameters (for example V_{s30} and κ). It is suggested that these near-surface parameters might exhibit strong correlations with geological features at greater depths, like basin depth parameters (Z_{xx}) (Chiou & Youngs, 2014; Kamai et al., 2016; Tsai et al., 2021), and consequently the amplification. However, opposing studies show that the amplification patterns might not necessarily correlate with these parameters (Castellaro et al., 2008; Mucciarelli & Gallipoli, 2006; Pitilakis et al., 2019), for example, sites with velocity profiles which are not monotonically increasing with depth. This highlights the necessity to investigate more regional geological structure to better understand the complexities of ground motion amplification.

Recently, the advances in computational capabilities and understanding the physical processes have made it possible to use physics-based (PB) simulations for modelling ground motions (Bradley, 2019; Graves & Pitarka, 2010; Smerzini & Villani, 2012; Taborda et al., 2014). PB simulations are carried out by numerical modelling of the entire process of rupture characterization and seismic wave propagation through the potentially complex Earth's crust. However, the high computational cost and complex input requirements associated with them restrict the large-scale usage of these methods, particularly in 3D. As a consequence the relative contribution of these processes to the total observed variability has been relatively unexplored compared to that of local shallow (decametre) site conditions.

The importance of robust ground motion modelling is particularly important during the current unprecedented global urbanization.The United Nations Human Settlements Programme (UN-Habitat) forecasts that by 2050 some 2 billion new citizens will move to urban centers so that, by then, some 68% of the world's population will live in cities (UN-Habitat, 2022). It is estimated that 95% of this urbanization will happen in the global south. Urban population growth is often accommodated by rapid urban expansion in areas with well-documented seismic risk. The problems of understanding and reducing disaster risk in such rapid development are significant, and while this expansion presents a major global challenge, it also provides a time-limited opportunity to provide evidence-based decision support for this new development (UNISDR, 2015). Efforts in earthquake risk reduction through urban planning guided by high-resolution ground-motion modelling, could reduce disaster risk for hundreds of millions of these future citizens. This approach also provides a cost-efficient method by concentrating on new constructions, where the expenses related to implementing effective earthquake-resistant design and construction are significantly lower compared to the costs of retrofitting at a later stage.

Two immediate problems emerge in enacting the current ground motion modelling approaches in the context of rapid urbanization in Global South,scheme described abovee in this context. Firstly, understanding ground motion requires extensive seismic databases recording appropriate measures of intensity from a large number of earthquakes, recorded at a network of sensors in the area of interest, for example, PEER-NGA databases (Ancheta et al., 2014; Atkinson & Boore, 2006; Spudich et al., 2013). Such catalogues necessitate the deployment of seismometers for many years even in the most seismically active areas that is not possible to address the current time-critical problem (Freddi et al., 2021). Secondly, urban development projects require hazard information at unusually high resolution. Urban flood modelling and landslide susceptibility estimates, for example, typically strive to use digital terrain models with 2-meter resolution supplemented by high-resolution geotechnical assessments (Jenkins et al., 2023). Seismic intensity also varies significantly over the scale of interest for urban planning, particularly where development is planned over sedimentary basins or near to coasts or rivers with strong spatial contrasts in sub-surface seismic velocity (Bielak et al., 1999; see also, Cadet et al., 2011; Foti et al., 2019).

Modellers have recognized the difficulties associated with the variability of ground motion at small scales, which can be attributed to local geological factors e.g. sedimentary basins (Graves

~~et al., 1998; Pilz et al., 2011; Zhu et al., 2018), surface topography (Lee et al., 2009; Maufroy et al., 2012; G. Wang et al., 2018), and soil conditions (Bazzurro & Cornell, 2004b; Cramer, 2003; Torre et al., 2020).~~ ~~In this study, we focus on the effects only due to the sedimentary basins, which are known to enhance the amplitude and duration of seismic waves through frequency-dependent focusing, trapping and resonance (Frankel, 1993; Yomogida & Etgen, 1993).~~ Some~~The~~ efforts have been made to incorporate these factors into GMPEs (Abrahamson et al., 2014; Campbell & Bozorgnia, 2014; Chiou & Youngs, 2014; Marafi et al., 2017), however, the extensive information required to accurately characterize such effects ~~such basin-specific amplification~~ remains a challenge.

As a result, the potential for high cost-benefit risk reduction that would accrue from high-resolution understanding of ground motion variability remains elusive. Typically, GMMs developed in data-rich countries of the global north are reconditioned for deployment in areas for which they have no obvious physical validity (Hough et al., 2016; Nath & Thingbaijam, 2011). At best, this leads to poor spatial resolution precluding the detailed site classification that is critical for seismic microzonation studies needed for cost-effective urban planning (Ansal et al., 2010). The development of appropriate techniques for rapid, local, high-resolution seismic hazard assessment is a significant global challenge.

In this research, we approach this challenge by using a simplified decomposition of ground motions into parametric relations explaining the regional and local variations in the measured intensity. We focus on the effects only due to the sedimentary basins, which are known to enhance the amplitude and duration of seismic waves through frequency-dependent focusing, trapping and resonance (Castellaro & Musinu, 2023; Frankel, 1993; Yomogida & Etgen, 1993). We demonstrate the usefulness of PB simulations in capturing the primary low frequency (LF), <1Hz, sedimentary basin effects that contribute to the variation in ground motion within an *urban* area situated within a seismically active region. We show, to first order, seismic intensity decays along the wave path according to the integrated rheological properties of the region and is concurrently subject to relative amplification specific to any point on the surface. We first provide the theoretical physical basis for the decomposition and then describe the simulation domain and the numerical scheme used to explore it. We then describe how the main elements of the problem, i.e., -regional mean field attenuation (Δ) and local sie-specific amplification (A) (explained in the subsequent section), can be extracted from the simulations and demonstrate their use in the ~~the convergence of the simulated ground motions providing measureable fields (Δ and A, explained in the subsequent section) that allow the~~ reconstruction of ~~the~~ originally simulated intensities. W~~W~~e highlight that the assessment of these reconstructed intensities~~parameters~~ is not notably influenced by source characteristics (such as location and directivity). Therefore, calibrating these parameters and understanding short-scale ground motion amplification variability can address the challenge posed by the lack of earthquake data. We suggest that this approach, when extended to including Higher Frequencies (HF), might provide an improved relative seismic risk assessment in the form of more reliable microzonation maps at the scale of urban planning, which is based on rapid seismological site characterization in the absence of long duration seismic catalogues.

2 Theoretical considerations

Using the seismic representation theorem, (De Hoop, 1958; Knopoff, 1956), in polar coordinates the displacement $\boldsymbol{U}_{\boldsymbol{\delta},\boldsymbol{\varepsilon}}$ recorded at a site $\boldsymbol{\varepsilon}$ for a point-source earthquake $\boldsymbol{\delta}$ is given by:

$$\boldsymbol{U}_{\boldsymbol{\delta},\boldsymbol{\varepsilon}} = \boldsymbol{G}_{\boldsymbol{\delta}(\boldsymbol{r},\boldsymbol{\theta},\emptyset),\boldsymbol{\varepsilon}} * \boldsymbol{f}_{\boldsymbol{\delta}(\boldsymbol{r},\boldsymbol{\theta},\emptyset)} \qquad (2)$$

Where, $\boldsymbol{r}$ is the distance between source and receiver, and $\boldsymbol{\theta}$ and $\emptyset$ are the positional angles in a spherical coordinate system, $\boldsymbol{f}_{\boldsymbol{\delta}}$ is a force vector at $\boldsymbol{\delta}$ and $\boldsymbol{G}$ is the elastodynamic Green's function providing the displacement at $\boldsymbol{\varepsilon}$ due to $\boldsymbol{f}_{\boldsymbol{\delta}}$. Since we consider the peak displacement in elastic medium ~~rather than a displacement time series~~ in what follows, this equation is time invariant.

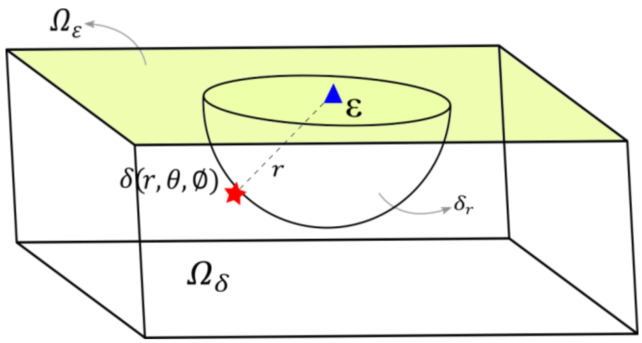

Figure 1: A cuboidal domain having a receiver at $\boldsymbol{\varepsilon}$ *and a seismic point source at* $\boldsymbol{\delta(r, \theta, \emptyset)}$*. The top surface of this domain represents receiver field* $\boldsymbol{\Omega_\varepsilon}$ *and the volume defines a source field* $\boldsymbol{\Omega_\delta}$*. All sources at a distance* $\boldsymbol{r}$ *from* $\boldsymbol{\varepsilon}$ *can be represented as the surface of hemisphere* $\boldsymbol{\delta_r}$*. These ground motion intensity at* $\boldsymbol{\varepsilon}$ *due to these sources are integrated in equation 3. This can further be integrated for all receivers at the surface* $\boldsymbol{\Omega_\varepsilon}$*, as calculated in equation 4.*

Consider a receiver at point $\boldsymbol{\varepsilon}$ that experiences displacements due to sources of a given seismic moment at a point $\boldsymbol{\delta}$ (see Figure 1). The average logarithm of the peak displacement field for all possible point sources $\boldsymbol{\delta_r}$ at distance $\boldsymbol{r}$ from the receiver $\boldsymbol{\varepsilon}$ can then be expressed as-

$$\overline{\ln\left(U_{\delta_r \varepsilon}\right)} = \frac{1}{2\pi^2} \int_0^{\pi} \int_0^{2\pi} \ln\left(U_{\delta(r,\theta,\emptyset),\varepsilon}\right) d\theta d\emptyset \quad (3)$$

$\overline{\ln\left(U_{\delta_r \varepsilon}\right)}$ then represents the expectation value for the intensity at $\boldsymbol{\varepsilon}$ due to all possible events at distance r. In this formulation, we consider point sources without any particular focal mechanism, so equation 3 might be considered as an integration over all possible focal mechanisms at all possible points on the hemisphere.

Integrating over all receivers $\boldsymbol{\Omega_\varepsilon}$ on the surface of the domain:

$$\overline{\ln\left(U_{(\delta\varepsilon)_r}\right)} = \frac{1}{\Omega_\varepsilon} \iint_{\Omega_\varepsilon} \overline{\ln\left(U_{\delta_r \varepsilon}\right)} \, d\varepsilon \quad (4)$$

then provides a mean field estimate of the expected intensity for any source-receiver pair separated by the distance $\boldsymbol{r}$, and a graph of $\overline{\mathbf{ln}\ (\mathbf{U}_{(\delta\varepsilon)_r})}$ against $\boldsymbol{r}$, represents the mean field decay of intensity with distance throughout the entire volume.

The response at a particular location on the surface to any specific event at some distance $\boldsymbol{r}$ will, of course, be subject to the source, path and site effects, all contributing to some local modification of the mean field expectation. Consider the ground motion at a receiver $\boldsymbol{\varepsilon}$ due to any source $\boldsymbol{\delta}$, again, the peak displacement ($\boldsymbol{U}_{\delta,\varepsilon}$) can be calculated using the representation theorem, this time giving:

$$\boldsymbol{U}_{\delta,\varepsilon} = \boldsymbol{G}_{\delta,\varepsilon} * \boldsymbol{f}_{\delta} \quad (5)$$

This peak ground displacement $\boldsymbol{U}_{\delta,\varepsilon}$ varies with $\boldsymbol{\varepsilon}$ but from Equation 4, we know its mean across the surface is $\overline{\mathbf{ln}\ (\mathbf{U}_{(\delta\varepsilon)_r})}$. Normalising the $\boldsymbol{U}_{\delta,\varepsilon}$ by $\overline{\mathbf{ln}\ (\mathbf{U}_{(\delta\varepsilon)_r})}$ removes the mean field decay leading to a normalised displacement $\widehat{\boldsymbol{U}_{\delta,\varepsilon}}$ given by:

$$\widehat{\boldsymbol{U}_{\delta,\varepsilon}} = {\boldsymbol{U}_{\delta,\varepsilon}} \Big/ {\overline{\mathbf{ln}\ (\mathbf{U}_{(\delta\varepsilon)_r})}} \quad (6)$$

Finally, to encapsulate the effect of all possible sources at each receiver, this normalised displacement can be integrated for the entire source field ($\boldsymbol{\Omega}_{\delta}$) , giving:

$$\overline{\mathbf{ln}\left(\widehat{\boldsymbol{U}_{\varepsilon}}\right)} = \frac{\mathbf{1}}{\boldsymbol{\Omega}_{\delta}} \iiint_{\boldsymbol{\Omega}_{\delta}} \mathbf{ln}\left(\widehat{\boldsymbol{U}_{\delta,\varepsilon}}\right) \boldsymbol{d\delta} \quad (7)$$

This $\overline{\mathbf{ln}\ (\widehat{\boldsymbol{U}_{\varepsilon}})}$ describes a local normalised amplification expected at any point for all possible sources. This can be considered as the integrated effect of the whole wave path from all possible sources that is dominated near $\boldsymbol{\varepsilon}$ where these paths converge. This term introduces the empirical site-specific variability using the normalised intensity of a suite of earthquakes of any magnitude.

Equations 4 and 7 now allow us to express the final estimate of intensity measure as:

$$\mathbf{ln}(\boldsymbol{IM}) = \overline{\mathbf{ln}\ (\boldsymbol{U}_{(\delta\varepsilon)_r})} + \overline{\mathbf{ln}\left(\widehat{\boldsymbol{U}_{\varepsilon}}\right)} \quad (8)$$

For the sake of simplicity, for an event at *i*, observed at a location $\boldsymbol{j}$, separated by a distance $\boldsymbol{r}$, $\boldsymbol{ln}\Delta_{\boldsymbol{r}}$ is used to denote the first term, the mean intensity decay $\overline{\mathbf{ln}\,(\boldsymbol{U}_{(\delta\varepsilon)_r})}$ and $\mathbf{ln}\boldsymbol{A_j}$ defines the second term describing amplification, $\overline{\mathbf{ln}\,(\widehat{\boldsymbol{U}_{\varepsilon}})}$. Now, equation 8 can then be re-written as:

$$\boldsymbol{IM_{i,j}} = \Delta_{\boldsymbol{r}} * \boldsymbol{A_j} \qquad \mathbf{(9)}$$

Where $\boldsymbol{IM_{ij}}$ is a non-specific intensity measure recognising that the argument so far may be generalised to peak velocity or acceleration. $\boldsymbol{IM_{ij}}$ then, provides an estimate of the intensity of ground motion based on the mean field expected intensity at a distance $\Delta_{\boldsymbol{r}}$, integrated over the entire crustal volume under consideration, and a relative amplification $\boldsymbol{A_j}$ due to the integrated effect of the seismic velocity structure around the site. Both terms on the right hand side are properties of the crust, regionally and locally, and do not include extended descriptions of the earthquake source, as we show in the next section. Equation 9 defines the $\Delta - \boldsymbol{A}$ decomposition, a static ground motion model that emphasises local geology rather than the descriptions of the earthquake source.

In practice, the mean field Δ and amplification $\boldsymbol{A}$, can both be calibrated through simulation based estimates for a given domain, hence the basis is essentially non-ergodic, but it is different than data-based statistically estimated parameters used in typical non-ergodic GMM (e.g. Landwehr *et al.*, 2016; Kuehn, Abrahamson and Walling, 2019). The spatial coefficients estimated in these non-ergodic model are data-dependent, hence in order to find potential drivers of GM variability in data sparse regions, there is very little scope to use these models. To clarify, the motivation for the potential utility of Δ-$\boldsymbol{A}$ method is to target the data-sparse regions without extensive availability of earthquake catalogues.

3 Defining Domain and source scenarios for simulations

To explore the behavior and stability of Δ and $\boldsymbol{A}$ (in equation 9) and how they might be estimated in practice, we use a virtual world that allows the exploration of the ideas in the absence of uncertainty but which allows the introduction of precisely constrained variability. We use a virtual crustal environment, as shown in Figure 2 (a,b), that incorporates a simplified subsurface velocity structure centered on a shallow and a deep river basin overlying a crystalline basement to which simplified velocities have been assigned. The description of the domain includes depth varying density ($\boldsymbol{\rho}$) , shear wave speed ($\boldsymbol{V_s}$), primary wave speed ($\boldsymbol{V_p}$), and anelastic attenuation factors ($\boldsymbol{Q_p}, \boldsymbol{Q_s}$), and is determined based on the assumed values of these parameters at the surface of the shallow basin (river channel), deep basin and basement (Brocher, 2005, 2008). The reader is referred to the Jenkins *et al.*, 2023, section 3.1 for detailed description for crustal domain and earthquake moment distribution. Alternatively, this information is also accessible in the supplementary materials (Table S1 and Figure S1).

In the middle of crustal domain, we locate a virtual urban environment Tomorrowville (Cremen et al., 2023; Gentile et al., 2022; Jenkins et al., 2023; Menteşe et al., 2023; C. Wang et al., 2023). The geology of Tomorrowville is based on a stretch of the Nakhu river valley on the outskirts of Lalitpur to the south of Kathmandu though the velocity structure described here extends far to the north and south, and does not represent the actual subsurface seismic velocity in the area. Instead, we simply generate a hypothetical near-surface velocity structure representative of any urban settlement located around a river channel set in a deeper and wider sedimentary basin. The depths of shallow and deep basins in Tomorrowville are presented in Figure 2 (c,d).

The random distribution of 40 thrust-faulting earthquakes~~events~~ (EQ1 to EQ20 are $\boldsymbol{Mw6}$ and EQ21 to EQ40 are $\boldsymbol{Mw5}$) is simulated across the domain (see Figure 2 e,f) using an established physics based solver, SPEED, which uses Spectral Element Method (SEM) for solving the wave-propagation equations ~~.~~(Mazzieri, Stupazzini, Guidotti, & Smerzini, 2013; Paolucci et al., 2014; Smerzini et al., 2011). The SEM combines the geometrical flexibility of the Finite Elements Method (FEM), i.e., the capability to naturally account for irregular interfaces and mesh adaptivity, with the high spectral accuracy, i.e., the exponential convergence rate to the exact solution that results in a fewer number of grid points per wavelength to maintain low dispersion. The crustal domain has a minimum shear wave velocity of 250 m/s and the smallest element size of 200m with the spectral degree of 4, hence, the simulations are able to resolve for the vibrational periods greater than 0.8s. Fault plane dimensions are determined using widely used empirical relationships developed by Wells & Coppersmith, 1994. ~~-~~Kinematic characterisation of rupture model is done based on the model developed by Liu et al., 2006; Schmedes et al., 2013 in which the correlation between the slip, rise time, peak time and rupture velocity among the sub-faults are derived based on a large ensemble of dynamic rupture simulations of dipping faults.

The moment distribution remains same for each magnitude ensemble, but the strike and dip are varied. -This distribution of rupture scenarios produce a wide range of expected source directivity for any location. The Peak Ground Acceleration (PGA) maps shown in Figure S2 and Movie S14, are referred for the visualisation of source orientation and their corresponding effects across the surface of entire domain. The wavefront evolution for EQ1 can also be found in Movies S21, S32 and S43 of the supplementary information as well.

The Δ-$\boldsymbol{A}$ decomposition, developed theoretically above (Section 2), includes no source variability whereas any attempt to understand seismic hazard must. The azimuth of the events from the seismometer with respect to the dominant velocity anisotropy introduced by the river basin will also contribute to the expected ground motion variability. The aim of this manuscript is not to examine the influence of these features on the observed local intensity; that will follow in a later work. Instead, we simply explore the extent to which the relative amplification term, $\boldsymbol{A_j}$, might act as a usable proxy that, to first order, governs the intensity variation across an urban area, irrespective of the source orientation. This might be considered as a lower bound on the skill of equation 9 in providing the basis for a static site-dependent ground motion model that might be improved later by the introduction of a source term to be constrained by the structural fabric and stress state around any specific location.

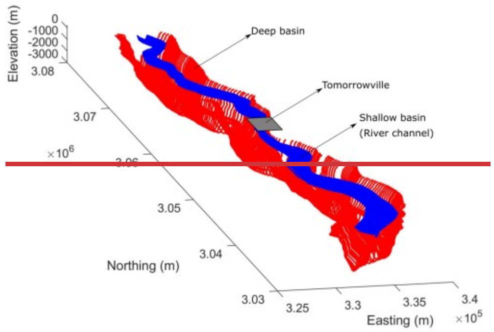
Elevation (m)
Deep basin
Tomorrowville
Shallow basin (River channel)
Northing (m)
Easting (m)

~~a)~~

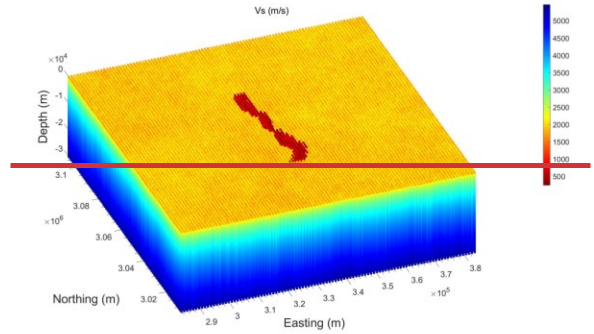
Vs (m/s)
Depth (m)
Northing (m)
Easting (m)

~~b)~~

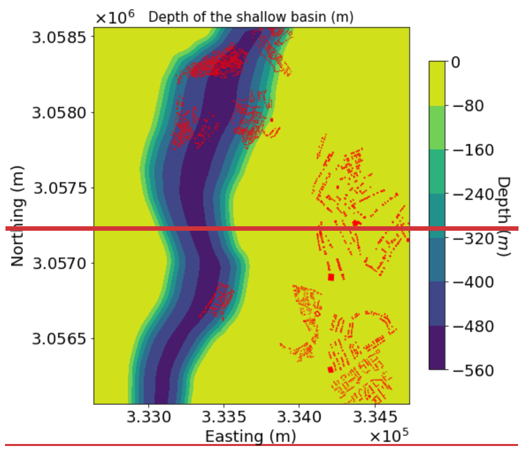
Depth of the shallow basin (m)
Northing (m)
Easting (m)
Depth (m)

~~(c)~~

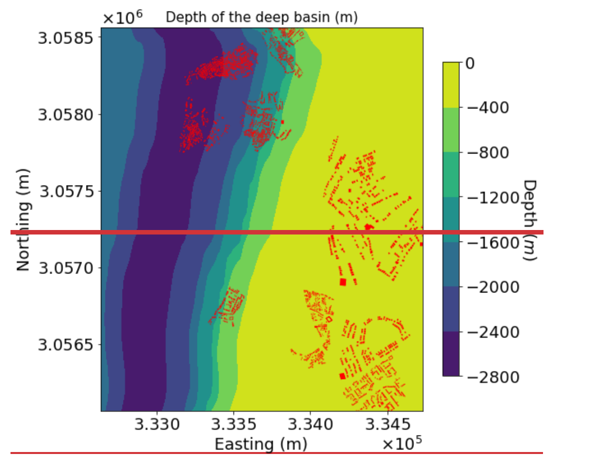
Depth of the deep basin (m)
Northing (m)
Easting (m)
Depth (m)

~~d)~~

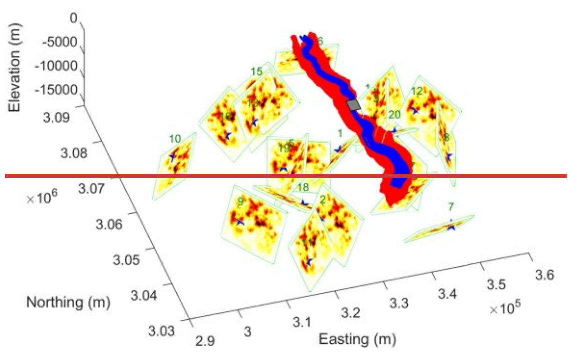
Elevation (m)
Northing (m)
Easting (m)

~~(e)~~

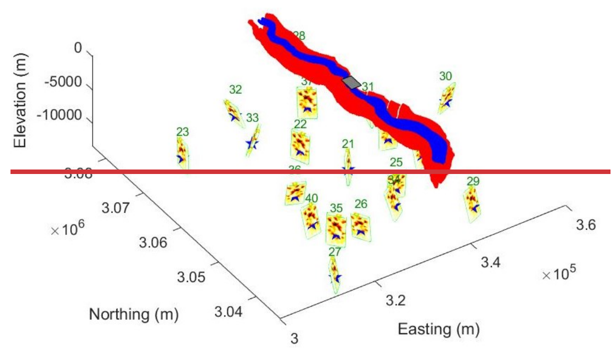
Elevation (m)
Northing (m)
Easting (m)

~~(f)~~

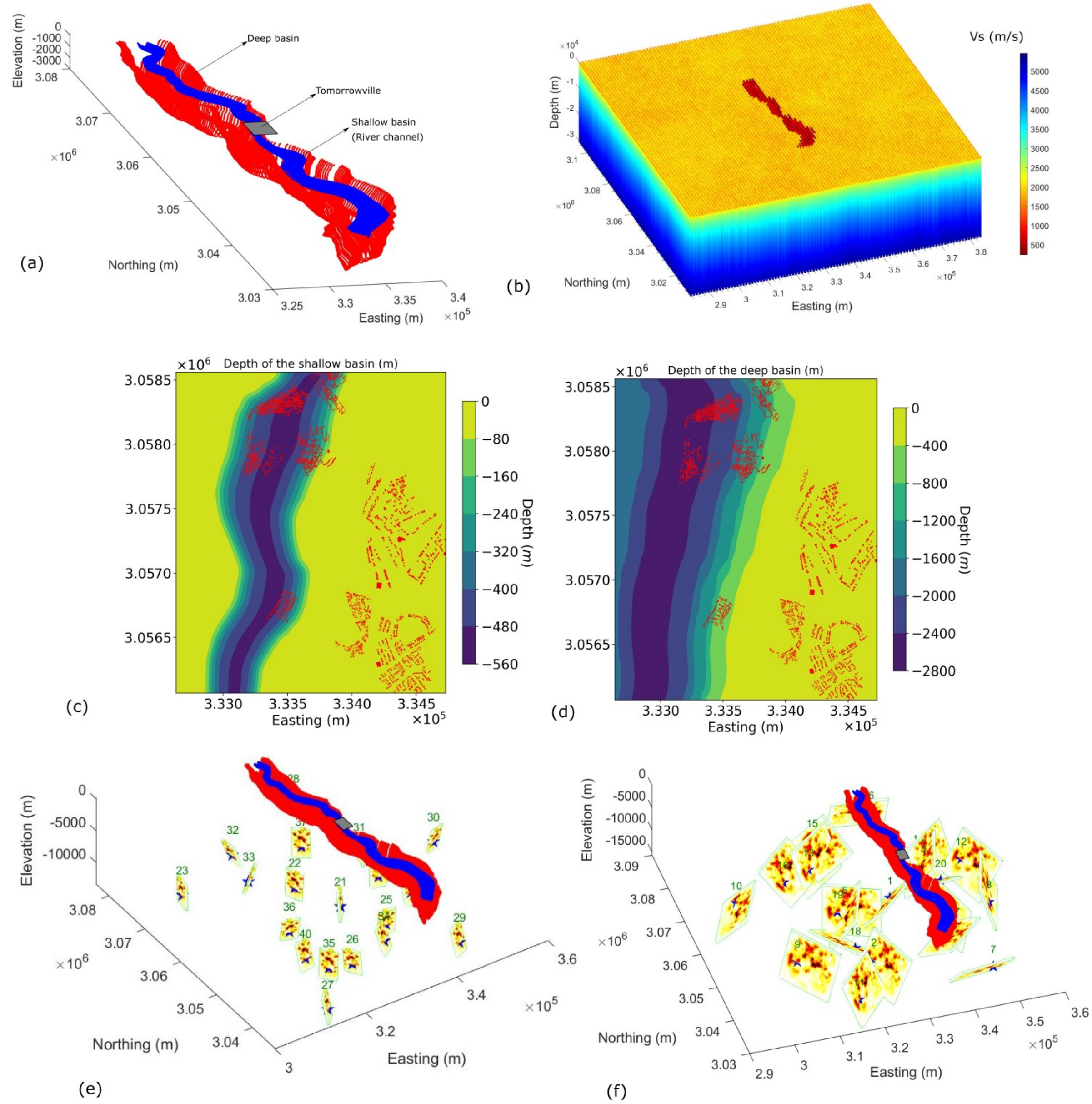

Figure 2: The computational domain used for the simulations and the distribution of earthquake scenarios is shown. a) The sedimentary basin structure showing a river channel creating a shallow basin of maximum depth 500m located inside a 2km deep basin (see Jenkins et al., 2023 for details). The gray rectangle represents Tomorrowville (eg. Cremen et al., 2022, Mentese et al., 2022), which has been designed to help understand the implications of development decision making on consequent risk to future communities. b) Represents the extent of the basin geometries using the shear wave velocities in a crustal volume of dimensions 100 km in length, 100km in width and 30km in depth. c) and d) show the basin depths of shallow and deep basins

across Tomorrowville with buildings distribution (red polygons). The building distribution is shown to highlight the direct impact of seismicity across the potential future infrastructure. e) and f) show 40 thrust earthquakes with random distributions of dip, rake and strike with EQ21 to EQ4~~2~~0 of $\boldsymbol{Mw}$**5~~6~~** *and EQ~~2~~1 to EQ2~~4~~0 of* $\boldsymbol{Mw}$**6~~5~~** *are generated across the domain. The hypocentres are represented by blue stars on the fault surface. The colour distribution across each rupture surface shows the moment release following the kinematic rupture models as developed by Liu et al., 2006; Schmedes et al., 2013.*

4 Estimation of Δ and $\boldsymbol{A}$ for Tomorrowville

The simulation results are used to estimate the Δ for the crustal domain and $\boldsymbol{A}$ for Tomorrowville (equation 9). The geometric mean of horizontal components of PGA values are used as intensity measure for all of the rupture scenarios. ~~The crustal domain has a minimum shear wave velocity of 250 m/s and the smallest element size of 200m with the spectral degree of 4, hence, the simulations are able to resolve for the vibrational periods greater than 0.8s.~~

To calculate $\boldsymbol{\Delta}$, we uniformly sample the surface of crustal domain which is a practical and computationally inexpensive approach to approximate the integration in equation 4. In the entire simulation domain, a random set of 100 recording locations is chosen (see green triangles in Figure 3a) for which estimates of the PGA are simulated for every event, generating a large number of estimates of the peak amplitude for different epicentral distances giving the data points for magnitude 5 and 6 events shown in F~~f~~igure 3b. We use simple least squares regression to the decay equation:

$$|\Delta_{\boldsymbol{r}}| = \boldsymbol{a} + \boldsymbol{b} \times \boldsymbol{ln}(\boldsymbol{r} + \boldsymbol{c}) \qquad (\mathbf{10})$$

here, $|\Delta_{\boldsymbol{r}}|$ i~~$\Delta_{\boldsymbol{r}}$ i~~s an estimation of the mean field intensity measure $\Delta_{\boldsymbol{r}}$ (introduced in equation 9), $\boldsymbol{r}$ is the epicentral distance and a,b and c are the empirical parameters evaluated from the data fitting procedure which might be modified without loss of insight (Figure 3b). The choice of 100 recording locations for $|\boldsymbol{\Delta_r}|$ estimation can have inherent uncertainities based on the selection. For instance, if the stations are predominantly concentrated in the basin, it could result in higher intensities in Figure 3b, consequently causing an upward shift in the mean field curve. However, such a scenario would not uniform sample the entire domain as intended; hence, current choice of stations seem satisfactory.

It should be noted that the regression method chosen here does not distinguish the repeatable (within event) and non-repeatable (between events) effects, which is followed from the fact that each source used here is characteristically similar and is recorded at the exact same set of receivers. Assuming the entire domain has a homogeneous earthquake distribution, each recording is considered independent, irrespective of whether the seismic energy is originated from same or different sources. The concept of earthquake source homogeneity implies that in a scenario with limited prior knowledge of the tectonics in the area, a reverse faulting earthquake could potentially occur at any azimuth with respect to the city.

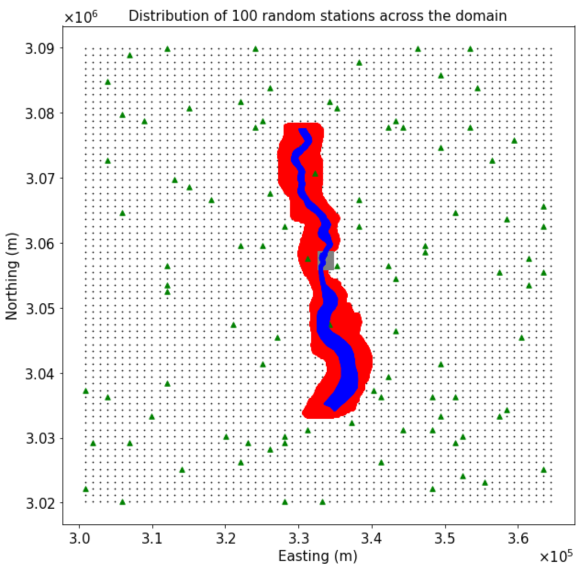

a)

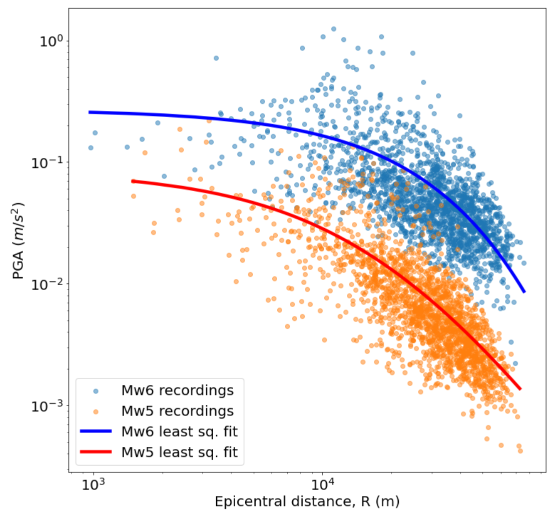

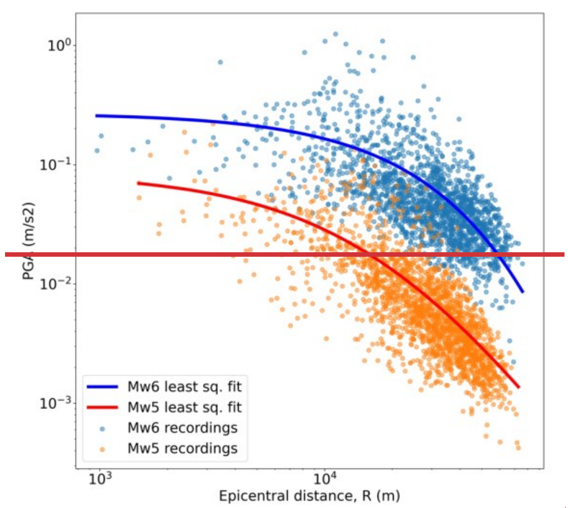

b)

b)

Formatte

Figure 3: a) A map of the computational domain showing the shallow basin (blue) created by river channel, and a deep basin (red), as well as the location of Tomorrowville (gray). Green triangles indicate the random locations of the 100 virtual seismometers. b) points indicate PGA versus epicentral distance for each of the 40 events at each virtual seismometer and the curves represents the least squares estimate of the mean field amplitude decay for this data.

We now must turn our attention to the variability of the data around the curves (Figure 3b) and will focus on the Tomorrowville sub-domain. Note, any numerical uncertainties due to the calculation, conditional on the input geological structure, are negligible compared to the variability observed in ~~figure~~Figure 3b. Hence, given the assumption that the simulation is providing accurate estimates in a virtual setting, each point in ~~figure~~Figure 3b accurately represents the local peak amplitude of waves from a particular event recorded at a single station. To estimate $|\boldsymbol{A_j}|$ for any location $\boldsymbol{j}$, the PGA values from all events are extracted for the Tomorrowville domain (Figure 4a~~e~~). Linear interpolation of intensities are used to provide these high-resolution maps, which sample Tomorrowville at an approximate grid spacing of 28 meters.

As an example, PGA from earthquake 1 (EQ1) is shown along with the spectral accelerations (5% damped) at 10 stations, S1 to S10 (Figure 4~~-~~b~~a~~,c~~b~~). Please note that these receivers are positioned within the Tomorrowville domain and are not accounted for in the wider receiver distribution illustrated in Figure 3a for the evaluation of $|\Delta_r|$. It can be clearly seen that the basin area is showing strong amplification resulting in higher PGA values due to wave trapping and resonance of the sedimentary basin layers, as compared to the lower PGA values along the areas of crystalline basement. Spectral accelerations at 10 stations show different orders of amplification over the entire period range (0.8s to 5s) corresponding to the geological locations of these stations. The consistent decrease in amplitude with increasing period observed at all stations indicates that it is majorly controlled by the selected source spectra. Stations S2, S3 and S7 lie in the combined (both deep and shallow) basin area and hence, recording maximum amplification, while the stations S1 and S6 lie above only deep basin area, hence the amplification is lesser but still significant at higher periods for all three components. The rest of the stations, S4, S5, S9 and S10 are situated over the basement rocks, hence recording the lowest value of spectral accelerations.

Our simulations focus on frequencies below 1Hz due to high computational costs associated with sampling higher frequencies in simulations. However, this analysis remains relevant since basins, like the Kathmandu basin, often exhibit resonance at similar frequencies (Asimaki et al., 2017; Oral et al., 2022). Additionally, when dealing with higher frequencies, it becomes necessary to account for other non-linear site effects that play a significant role in intensity variations (Semblat et al., 2005), which are not included in this analysis. More discussion on basin resonance is provided in the supplementary material Text S1.

Given the geometry of the basin stretched approximately North-South (NS) whilst being much more confined along East-West (EW), the amplification of both horizontal components should be theoretically contrasting. However, the periods resolved in the simulations suggest the inter-component variability is still lower than the inter-station variability across different geological domains (Figure 4b). This suggests, the geometric mean of the horizontal components of PGA at each station seem a usable guide to explore the amplification further discussed in this study.

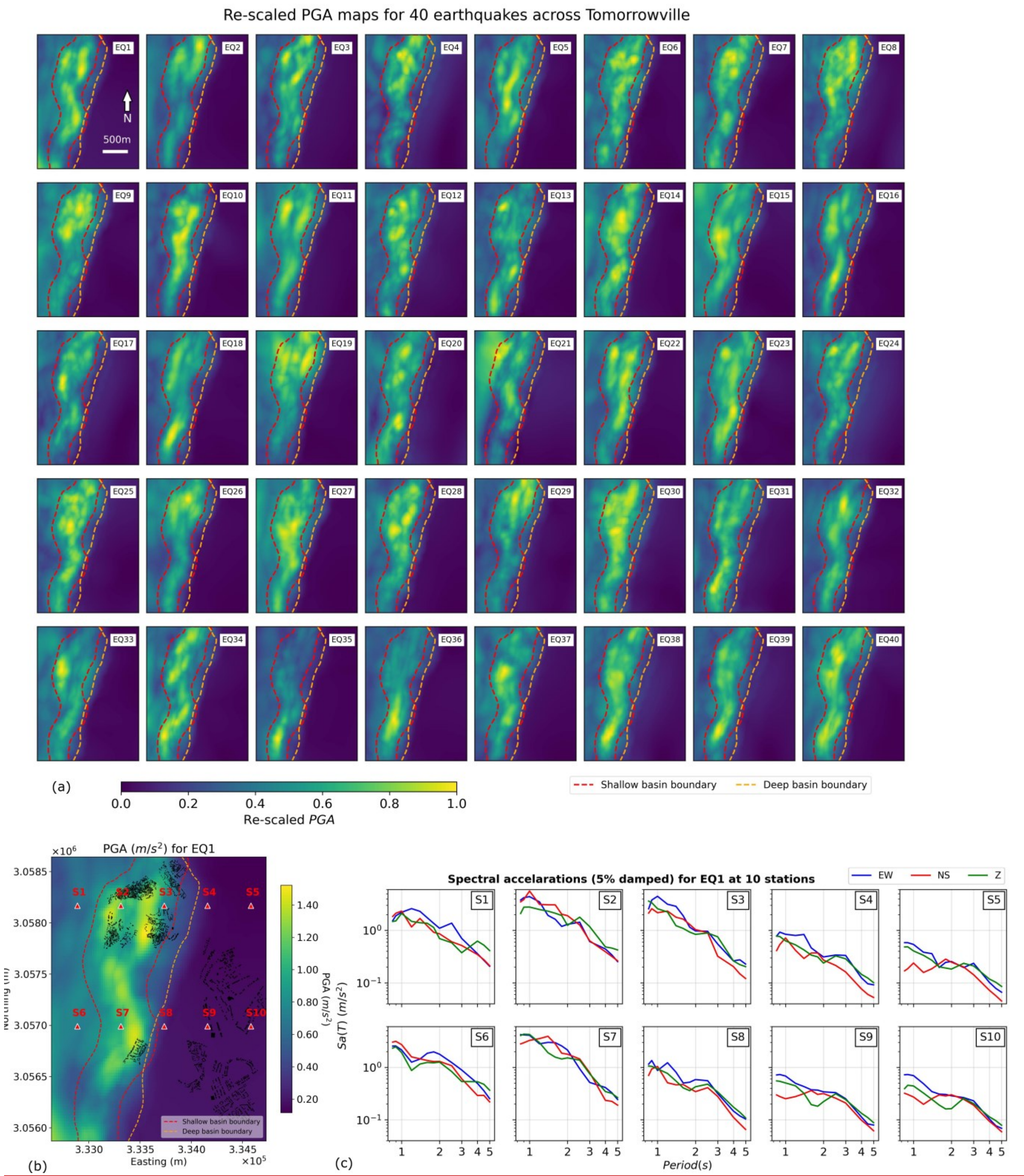

Figure 4: a) PGA maps for 40 events plotted on Tomorrowville city domain. EQ1 to EQ20 represent data from Mw6 earthquakes while EQ21 to EQ40 are for Mw5. Note that we have

scaled each map between 0 and 1, where 0 is minimum and 1 is maximum PGA for each earthquake. The similarity of the maps indicates that, to first order, regardless of the absolute value of the PGA across the zone, the relative amplitude for different locations is invariant. b) Shows the PGA (geometric mean of two horizontal components) values for EQ1 along with the boundaries of shallow and deep basins, represented by red and orange dashed lines, respectively. Red triangles show 10 stations, S1 to S10 that are used to show the spectral accelerations for the 0.8s to 5s in c). Three components East-West (EW), North-South (NS) and Vertical (Z) are plotted separately.

Given the geometry of the basin stretched approximately North-South (NS) whilst being much more confined along East-West (EW), the amplification of both horizontal components should be theoretically contrasting. However, the periods resolved in the simulations show the inter-component variability is still lower than the inter-station variability across different geological domains (Figure 4c). This suggests, the geometric mean of the horizontal components of PGA at each station seem a usable guide to explore the amplification further discussed in this study.

The pattern of higher amplification along the river basin and lower amplification along the basement area is common for PGA maps of all the earthquake scenarios (Figure 4ae). Hence while the absolute PGA is strongly dependent on the source magnitude and distance, the *relative* amplitude within any map is qualitatively independent of earthquake source orientation, and even magnitude. The structural similarity of PGA maps in Figure 4ae seems to indicate the potential utility of the Δ-***A*** decomposition.

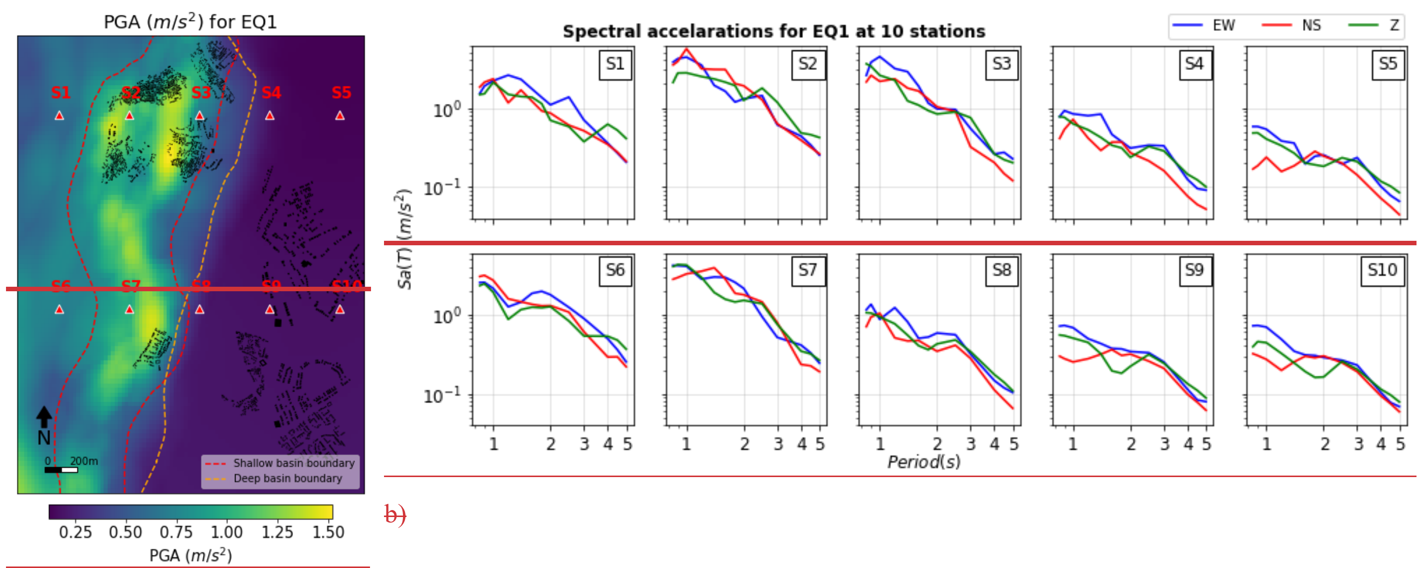

b)

a)

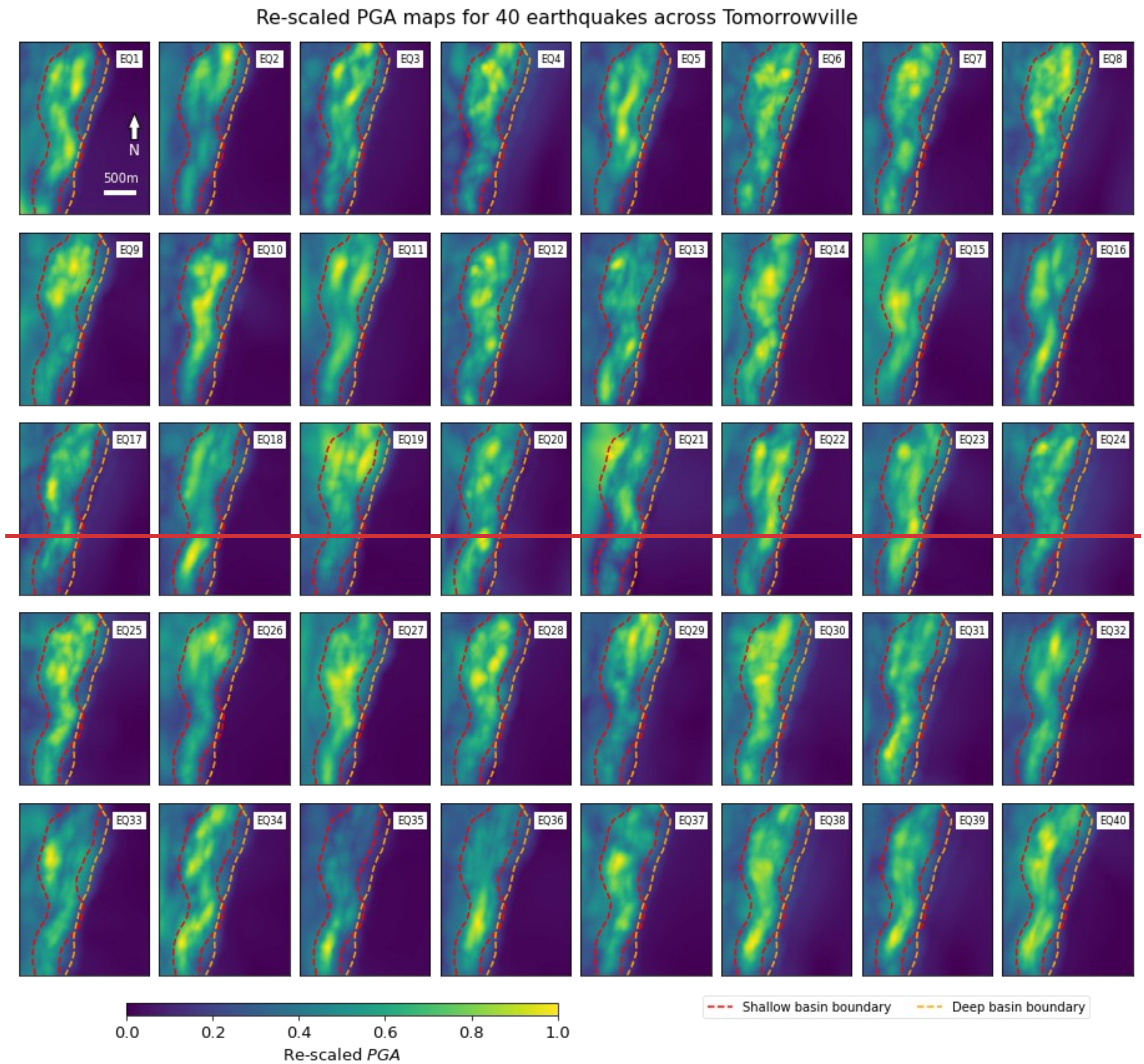

~~c)~~

~~*Figure 4: Simulation results are extracted for Tomorrowville domain. a) Shows the PGA (geometric mean of two horizontal components) values for EQ1 along with the boundaries of shallow and deep basins, represented by red and orange dashed lines, respectively. Red triangles show 10 stations, S1 to S10 that are used to show the spectral accelerations for the 0.8s to 5s in b). Three components East-West (EW), North-South (NS) and Vertical (Z) are plotted separately. c) PGA maps for 40 events plotted on TV city domain. EQ1 to EQ20 represent data from Mw6 earthquakes while EQ21 to EQ40 are for Mw5. Note that we have scaled each map between 0 and 1, where 0 is minimum and 1 is maximum PGA for each earthquake. The similarity of the*~~

~~maps indicates that, to first order, regardless of the absolute value of the PGA across the zone, the relative amplitude for different locations is invariant.~~

To extract this pervasive feature of relative amplification from all earthquake scenarios we normalise and stack the PGA maps for each event. First, all PGA maps are normalised using the mean smooth earth expectation value $|\Delta_{\boldsymbol{r}}|$, calculated from equation 10. This normalisation is the practical implementation from the theoretical description given in the equation 6, where the normalisation factor is taken as the mean intensity decay in equation 4. Let, $|\boldsymbol{U_{ij}}|$ be the simulated PGA at a particular site $\boldsymbol{j}$ due to an earthquake $\boldsymbol{i}$ at a distance $\boldsymbol{r}$, then the normalised PGA $\widehat{|\boldsymbol{U_{ij}}|}$ would be –

$$\widehat{|\boldsymbol{U_{ij}}|} = {|\boldsymbol{U_{ij}}|}/{|\Delta_{\boldsymbol{r}}|} \qquad (\mathbf{11})$$

After normalisation, the average PGA of the normalised maps is calculated for $\boldsymbol{N_e}$ number of earthquake scenarios, as described in equation 7. This final, averaged PGA map is a characteristic spatial kernel for the chosen city domain and theoretically contains the average local amplification $(\boldsymbol{A_j})$ at any site $\boldsymbol{j}$ for any possible earthquake regardless of source, (see Figure 5a). Here, $\boldsymbol{A_j}$ has the following form-

$$\boldsymbol{A_j} = \left(\prod_{\boldsymbol{i=1}}^{\boldsymbol{N_e}} \widehat{|\boldsymbol{U_{ij}}|}\right)^{\frac{\boldsymbol{1}}{\boldsymbol{N_e}}} \qquad (\mathbf{12})$$

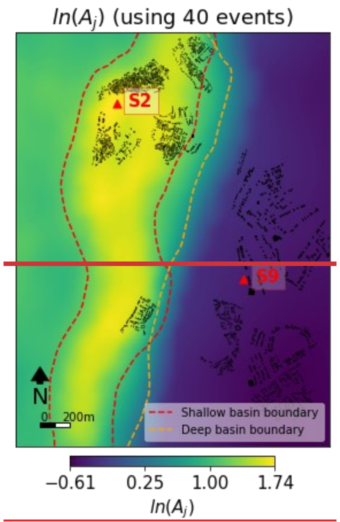

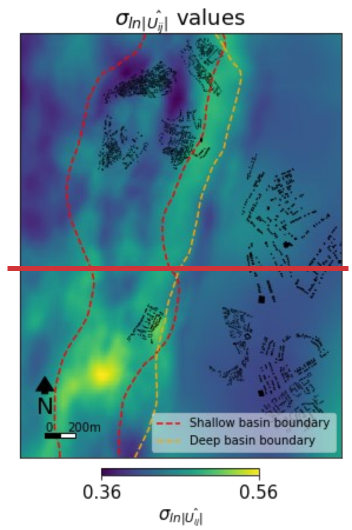

a)

b)

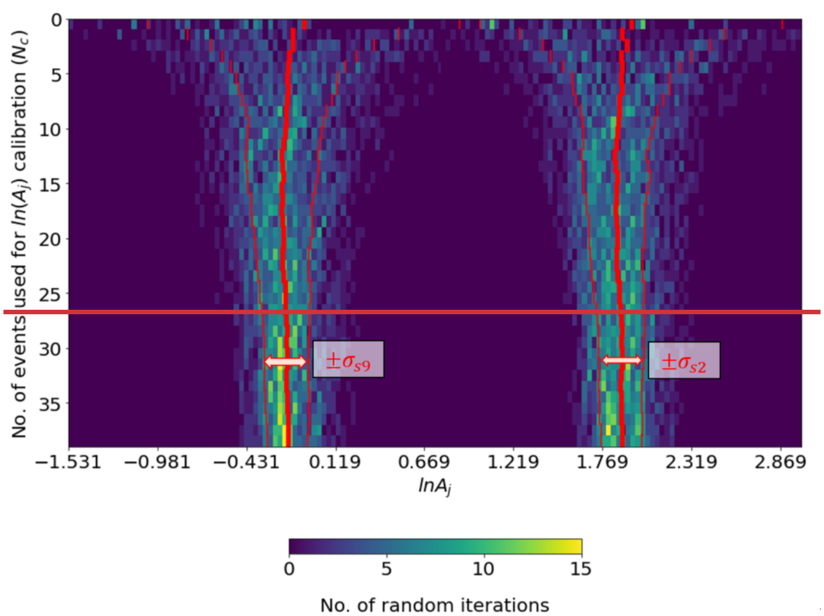

c)

Figure 5: a) Estimates of $\ln A_j$*, and b) the standard deviation (*$\sigma_{\ln|\widehat{U_{ij}}|}$*) for Tomorrowville. Two locations, one in the river basin (* ***S2****), and one where the crystalline basement outcrops at the surface at (****S9****) are chosen in a), to plot the convergence of the* $\ln A_j$ *at* ***S2*** *and* ***S9*** *with an increasing number of events as shown in c).*

The calculation of $\boldsymbol{A_j}$ results in a mean amplification field consistent with the spatial variations observed in the simulations (Figure 5a). Each pixel represents the mean amplification experienced at that location over all magnitudes, azimuths and directivity.

There is, of course, a dispersion of $\boldsymbol{ln\left|\widehat{U_{ij}}\right|}$ values around this mean which is itself a spatially variable field over the domain, calculated by the $\boldsymbol{\sigma_{ln\left|\widehat{U_{ij}}\right|}}$ (Figure 5b) as:

$$\boldsymbol{\sigma_{ln\left|\widehat{U_{ij}}\right|} = \sqrt{\frac{1}{N_e}\sum_{i=1}^{N_e}\left(ln\left|\widehat{U_{ij}}\right| - lnA_j\right)^2}} \qquad \textbf{(13)}$$

where, $\boldsymbol{\sigma_{ln\left|\widehat{U_{ij}}\right|}}$ gives the variability due to various source scenarios used in the analysis and the corresponding path effects. The maximum value of $\boldsymbol{\sigma_{ln\left|\widehat{U_{ij}}\right|}}$ is 0.56, that is 23.8% of the entire $\boldsymbol{lnA_j}$ range of 2.35 in Tomorrowville. The difference of 2.35 in maximum ($\boldsymbol{lnA_{j,max}}$) and minimum ($\boldsymbol{lnA_{j,min}}$) values would mean, the ratio $\boldsymbol{A_{j,max}/A_{j,min}}$ is $\boldsymbol{e^{2.35} \sim 10.48}$, implying an order of magnitude variation within Tomorrowville. Notably, the ranges of the amplification and standard deviations are of a realistic order often found in some of the extensively studied real-world settings as well, for example as shown by Day et al., 2019 in Southern California.

Another approach to understanding the variability of the amplification field involves varying the number of events used to calculate $\boldsymbol{lnA_j}$ and examining its variability at a specific location using the events selected through a bootstrapping approach. We chose two stations from Figure 4ba, one representing an area of high amplification over the river basin, named as $\boldsymbol{S2}$, and one in low amplification over outcropping basement, named as $\boldsymbol{S9}$ (see Figure 5a). The number of events $\boldsymbol{N_c}$, used to estimate $\boldsymbol{A_j}$, is plotted against the $\boldsymbol{lnA_j}$, where the colour intensity represents the distribution of the iterations across the entire $\boldsymbol{lnA_j}$ range (Figure 5c). For each $\boldsymbol{N_c}$ value, 100 random combination of events with repetition are used for $\boldsymbol{lnA_j}$ calculation. The red dashes correspond to the $\boldsymbol{\pm 1\ \sigma_{s2}}$ and $\boldsymbol{\pm 1\ \sigma_{s9}}$ variability around the mean $\boldsymbol{lnA_j}$ value for the respective $\boldsymbol{N_c}$ value. The convergence of the $\boldsymbol{lnA_j}$ values can be observed even with as low as ~7 events with a stable $\boldsymbol{\pm\sigma_{s2}}$ and $\boldsymbol{\pm\sigma_{s9}}$ around the $\boldsymbol{lnA_j}$ values of 0.12 each. This distribution of $\boldsymbol{lnA_j}$ is non-overlapping for both sites, ***S*2** and ***S*9**, which suggests that the local crustal features at both of these sites is the dominant contributor in the amplification.

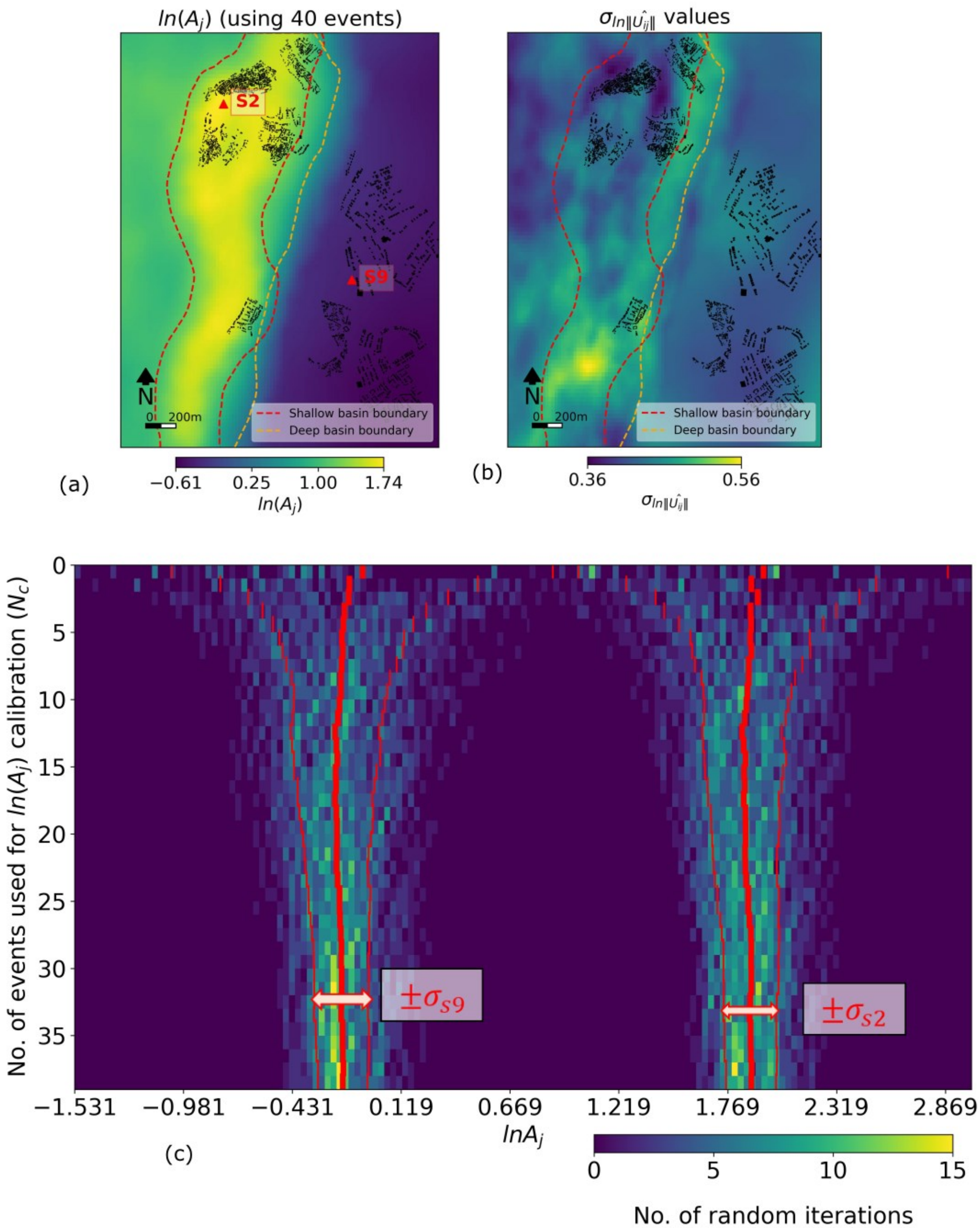

Figure 5: a) Estimates of $\mathbf{lnA_j}$, and b) the standard deviation ($\boldsymbol{\sigma}_{ln\left|\widehat{U_{ij}}\right|}$) for Tomorrowville. Two locations, one in the river basin ($\boldsymbol{S2}$), and one where the crystalline basement outcrops at the surface at ($\boldsymbol{S9}$) are chosen in a), to plot the convergence of the $\mathbf{lnA_j}$ at $\boldsymbol{S2}$ and $\boldsymbol{S9}$ with an increasing number of events as shown in c).

5 Estimation of PGA using Δ and A for 40 earthquakes

The theoretical treatment described in section 2 above suggests that the ground motion at a point can be decomposed into the effect of the mean field attenuation over the wave path integrated over the crustal volume and the effect of the local velocity structure. This implies that the reversal of this process should reproduce the original PGA field. Thus if we have robust estimates of Δ and $\boldsymbol{A}$, then we should be able to reproduce the intensity at any point using equation 9.

We demonstrate this process for a single earthquake, EQ13 located 30.4 km to the NW of Tomorrowville, we will show that the choice of the earthquake is not important. The simulated PGA at every point will be referred to as the true value, $\boldsymbol{PGA_{true}}$ (see Figure 6a,e). To estimate the PGA value explained in equation 9 for this event, referred herein as $\boldsymbol{PGA_{\Delta A}}$, we first calibrate the Δ (Figure 6b) and $\boldsymbol{A}$ (Figure 6c) using the rest of 39 simulated events. Δ and $\boldsymbol{A}$ are multiplied as shown in equation 9 to obtain $\boldsymbol{PGA_{\Delta A}}$ values for this earthquake (see Figure 6d). The difference between $\boldsymbol{PGA_{\Delta A}}$ and $\boldsymbol{PGA_{true}}$ is calculated and plotted as a residual map (see Figure 6f). The basin area shows higher negative residuals suggesting underestimation of $\boldsymbol{PGA_{\Delta A}}$ where $\boldsymbol{PGA_{true}}$ values are higher, while surrounding basement exhibits positive values, suggesting overestimation. A graph of $\boldsymbol{PGA_{\Delta A}}$ as a function of $\boldsymbol{PGA_{true}}$ is shown in F~~f~~igure 6g along with the histograms of all the grid points across Tomorrowville. There is a systematic overestimation of $\boldsymbol{PGA_{\Delta A}}$ values for this particular event at the lower PGA range, and a minor underestimation can be seen at the higher PGA side. This pattern can be attributed to the characteristic that the $\boldsymbol{lnA_j}$ values, which are used to calculate $\boldsymbol{PGA_{\Delta A}}$, have mean amplification values spanning a wider range compared to this specific event. Pearson correlation coefficient ($\boldsymbol{\gamma}$) between logarithms of $\boldsymbol{PGA_{\Delta A}}$ and $\boldsymbol{PGA_{true}}$ is 0.98, suggesting strong correlation between the two. The histograms presented in parallel to the axes also indicate that the distribution nature of PGA ~~Peak Ground Acceleration (PGA)~~ remains preserved across Tomorrowville, exhibiting a tri-modal pattern in both PGA_{true} and $PGA_{\Delta A}$ (Figure 6g). This tri-modal pattern is a distinctive influence of three geological domains in the city- the deep basin area (to the left of shallow basin boundary), the area comprising both deep and shallow basins, and the basement region.

Finally, For each event in the suite of 40 earthquakes, the remaining 39 simulations are used to calculate the Δ and A, that are multiplied to obtain $PGA_{\Delta A}$. The results are compared with the corresponding PGA_{true} of each earthquake using the γ value and best fitting regression line (Figure 7a). Lowest γ value is 0.89, which suggests the correlation is strong for all the earthquakes. In conclusion, there is a clear potential of predictability in $PGA_{\Delta A}$, with some variability translated from different source-specific variability due to heterogeneous moment distribution along the fault surface, as well as, path related variability due to azimuth of sources with respect to the Tomorrowville. This variability in $PGA_{\Delta A}$, is captured earlier using the $\sigma_{ln|\widehat{U_{ij}}|}$ values calculated in figure 5b.

The impact of source orientation on the obtained γ value is illustrated by examining three parameters: epicentral distance, back azimuth of the earthquake (bearing of the line joining hypocenter to the center of Tomorrowville), and the angle of approach (the azimuthal difference between the line connecting the hypocenter to the major fault asperity, and the line connecting the hypocenter to the center of Tomorrowville) (Figure 7b). The back-azimuth and angle of approach provide insights into the influence of horizontally anisotropic crustal domain and directivity effects resulting from variations in fault orientation relative to Tomorrowville, respectively. γ is observed to have a positive trend with the epicentral distance indicating that the the earthquakes closer to tomorrowville are poorly constrained by $PGA_{\Delta A}$ compared to the ones farther away. It can also be seen that the chosen earthquake distribution samples a wide range of back-azimuth and angle of approach values, indicating a comprehensive representation of these factors. γ does not show any notable trend with the these two factors, hence, their impact on estimating the distribution of PGA values across Tomorrowville is not substantial.

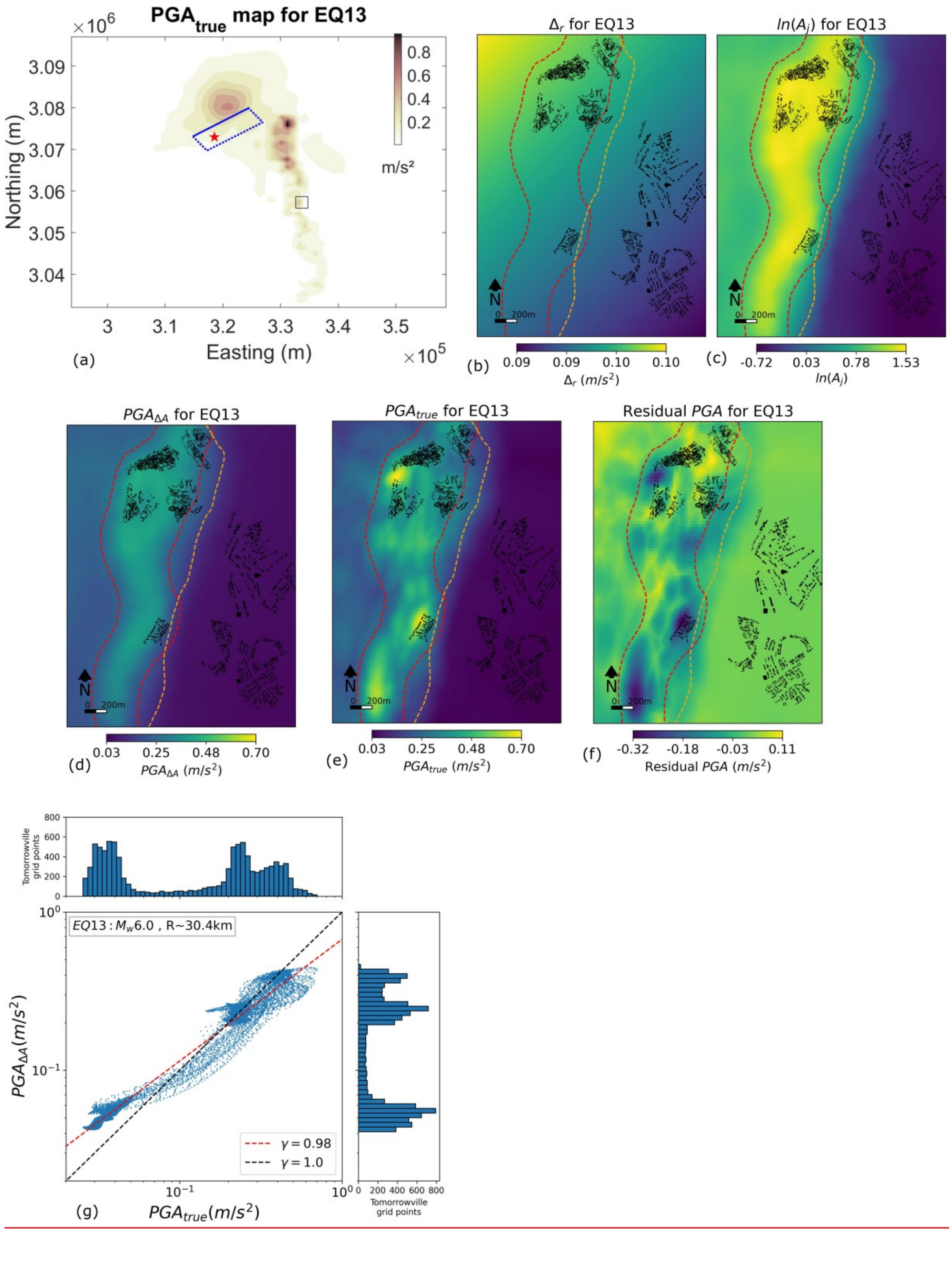

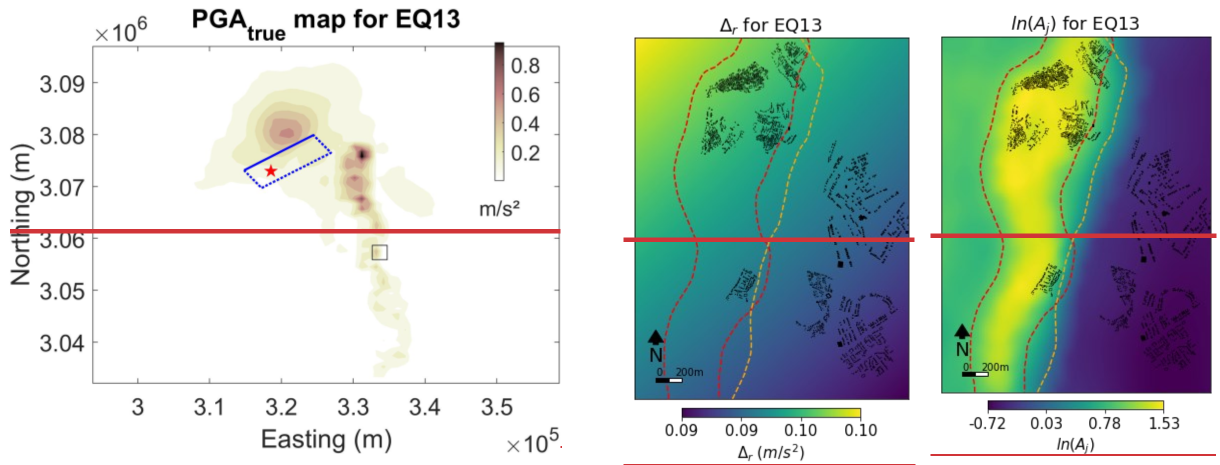
PGA$_{true}$ map for EQ13
$\times10^6$
3.09
3.08
3.07
3.06
3.05
3.04
Northing (m)
3
3.1
3.2
3.3
3.4
3.5
Easting (m)
$\times10^5$
0.8
0.6
0.4
0.2
m/s²
Δ_r for EQ13
N
0 200m
0.09 0.09 0.10 0.10
Δ_r (m/s^2)
$ln(A_j)$ for EQ13
-0.72 0.03 0.78 1.53
$ln(A_j)$

~~a)~~ ~~b)~~ ~~c)~~

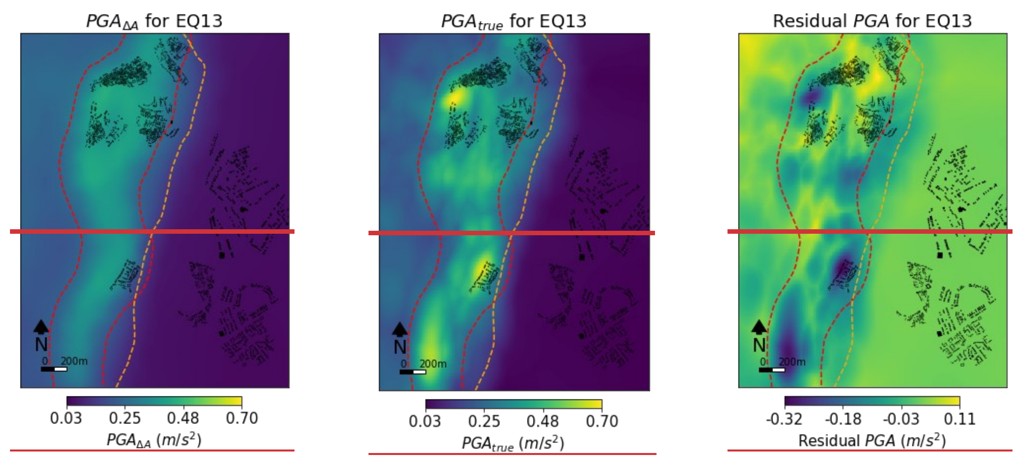
$PGA_{\Delta A}$ for EQ13
N
0 200m
0.03 0.25 0.48 0.70
$PGA_{\Delta A}$ (m/s^2)
PGA_{true} for EQ13
0.03 0.25 0.48 0.70
PGA_{true} (m/s^2)
Residual PGA for EQ13
-0.32 -0.18 -0.03 0.11
Residual PGA (m/s^2)

~~d)~~ ~~e)~~ ~~f)~~

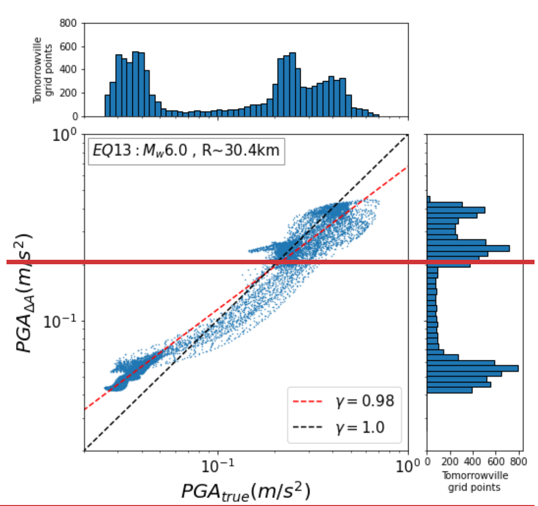
800
600
400
200
0
Tomorrowville grid points
$EQ13 : M_w6.0$, R~30.4km
10^0
10^{-1}
$PGA_{\Delta A}(m/s^2)$
$\gamma = 0.98$
$\gamma = 1.0$
10^{-1}
10^0
$PGA_{true}(m/s^2)$
0 200 400 600 800
Tomorrowville grid points

~~g)~~

Figure 6: Result showing estimated parameters for EQ13. a) $\boldsymbol{PGA_{true}}$ *map for EQ13 showing the simulation results across the entire crustal domain, the blue dashed-rectangle shows the location of rupture surface (top edge is solid blue), red star shows the hypocentre and black rectangle in the middle of domain shows the location of Tomorrowville. b) shows* $\Delta_{\boldsymbol{r}}$ *and c) shows* $\boldsymbol{lnA_j}$ *for event EQ13 for Tomorrowville. d) shows the* $\boldsymbol{PGA_{\Delta A}}$ *distribution calculated by multiplying* $\Delta_{\boldsymbol{r}}$ *with* $\boldsymbol{A_j}$ *as conceptualised in equation 9. e)* $\boldsymbol{PGA_{true}}$ *map for this event obtained through the PB simulation. f) residual between* $\boldsymbol{PGA_{\Delta A}}$ *and* $\boldsymbol{PGA_{true}}$ *g) shows the comparison between* $\boldsymbol{PGA_{\Delta A}}$ *and* $\boldsymbol{PGA_{true}}$ *for EQ13 using the Pearson correlation coefficient (*$\boldsymbol{\gamma}$*) of 0.98 for this event. Marginal panels show histograms of* $\boldsymbol{PGA_{\Delta A}}$ *(right) and* $\boldsymbol{PGA_{true}}$*(top) indicating the similarity in distribution of* $\boldsymbol{PGA}$ *values across Tomorrowville city domain.*

Finally, for each event in the suite of 40 earthquakes, the remaining 39 simulations are used to calculate the Δ and $\boldsymbol{A}$, that are multiplied to obtain $\boldsymbol{PGA_{\Delta A}}$. The results are compared with the corresponding $\boldsymbol{PGA_{true}}$ of each earthquake using the $\boldsymbol{\gamma}$ value and best fitting regression line (Figure 7a). Lowest $\boldsymbol{\gamma}$ value is 0.89, which suggests the correlation is strong for all the earthquakes. In conclusion, there is a clear potential of predictability in $\boldsymbol{PGA_{\Delta A}}$, with some variability translated from different source-specific variability due to heterogeneous moment distribution along the fault surface, as well as, path related variability due to azimuth of sources with respect to the Tomorrowville. This variability in $\boldsymbol{PGA_{\Delta A}}$, is captured earlier using the $\boldsymbol{\sigma_{ln\left|\widehat{U_{ij}}\right|}}$ values calculated in Figure 5b.

The impact of source orientation on the obtained $\boldsymbol{\gamma}$ value is illustrated by examining three parameters: epicentral distance, back azimuth of the earthquake (bearing of the line joining hypocenter to the center of Tomorrowville), and the angle of approach (the azimuthal difference between the line connecting the hypocenter to the major fault asperity, and the line connecting the hypocenter to the center of Tomorrowville) (Figure 7b). The back-azimuth and angle of approach provide insights into the influence of horizontally anisotropic crustal domain and directivity effects resulting from variations in fault orientation relative to Tomorrowville, respectively. $\boldsymbol{\gamma}$ is observed to have a positive trend with epicentral distance indicating that the earthquakes closer to tomorrowville are poorly constrained by $\boldsymbol{PGA_{\Delta A}}$ compared to the ones farther away. It can also be seen that the chosen earthquake distribution samples a wide range of back-azimuth and angle of approach values, indicating a comprehensive representation of these factors. γ does not show any notable trend with the these two factors, hence, their impact on estimating the distribution of PGA values across Tomorrowville is not substantial.

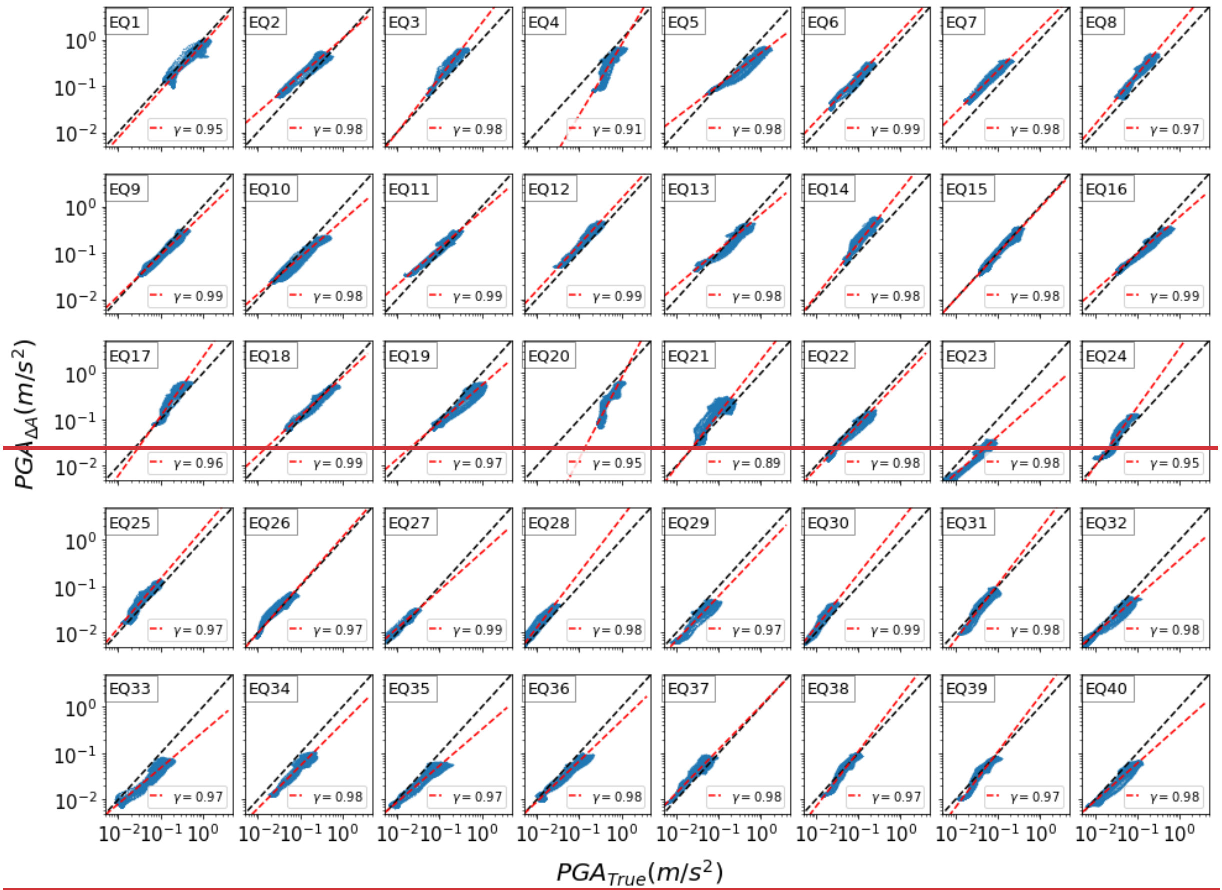

EQ1 γ= 0.95
EQ2 γ= 0.98
EQ3 γ= 0.98
EQ4 γ= 0.91
EQ5 γ= 0.98
EQ6 γ= 0.99
EQ7 γ= 0.98
EQ8 γ= 0.97
EQ9 γ= 0.99
EQ10 γ= 0.98
EQ11 γ= 0.99
EQ12 γ= 0.99
EQ13 γ= 0.98
EQ14 γ= 0.98
EQ15 γ= 0.98
EQ16 γ= 0.99
EQ17 γ= 0.96
EQ18 γ= 0.99
EQ19 γ= 0.97
EQ20 γ= 0.95
EQ21 γ= 0.89
EQ22 γ= 0.98
EQ23 γ= 0.98
EQ24 γ= 0.95
EQ25 γ= 0.97
EQ26 γ= 0.97
EQ27 γ= 0.99
EQ28 γ= 0.98
EQ29 γ= 0.97
EQ30 γ= 0.99
EQ31 γ= 0.98
EQ32 γ= 0.98
EQ33 γ= 0.97
EQ34 γ= 0.98
EQ35 γ= 0.97
EQ36 γ= 0.98
EQ37 γ= 0.98
EQ38 γ= 0.97
EQ39 γ= 0.97
EQ40 γ= 0.98
$PGA_{\Delta A}(m/s^2)$
$PGA_{True}(m/s^2)$

a)

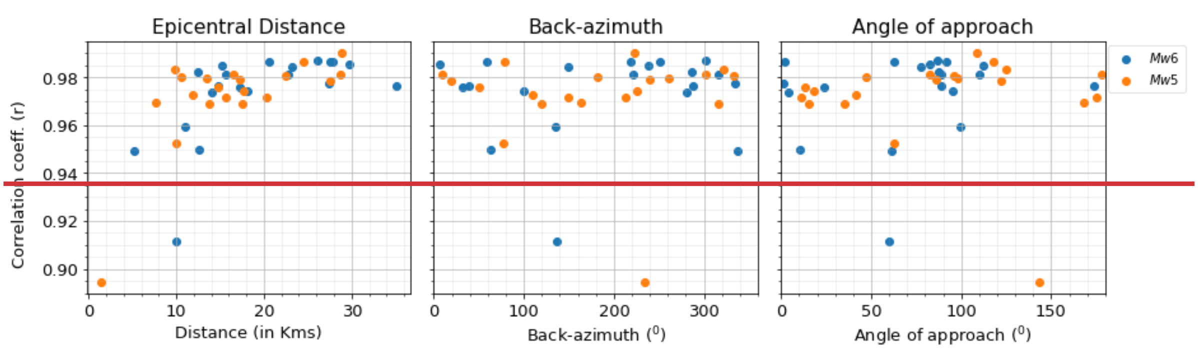

Epicentral Distance
Back-azimuth
Angle of approach
Correlation coeff. (r)
Distance (in Kms)
Back-azimuth (0)
Angle of approach (0)
Mw6
Mw5

b)

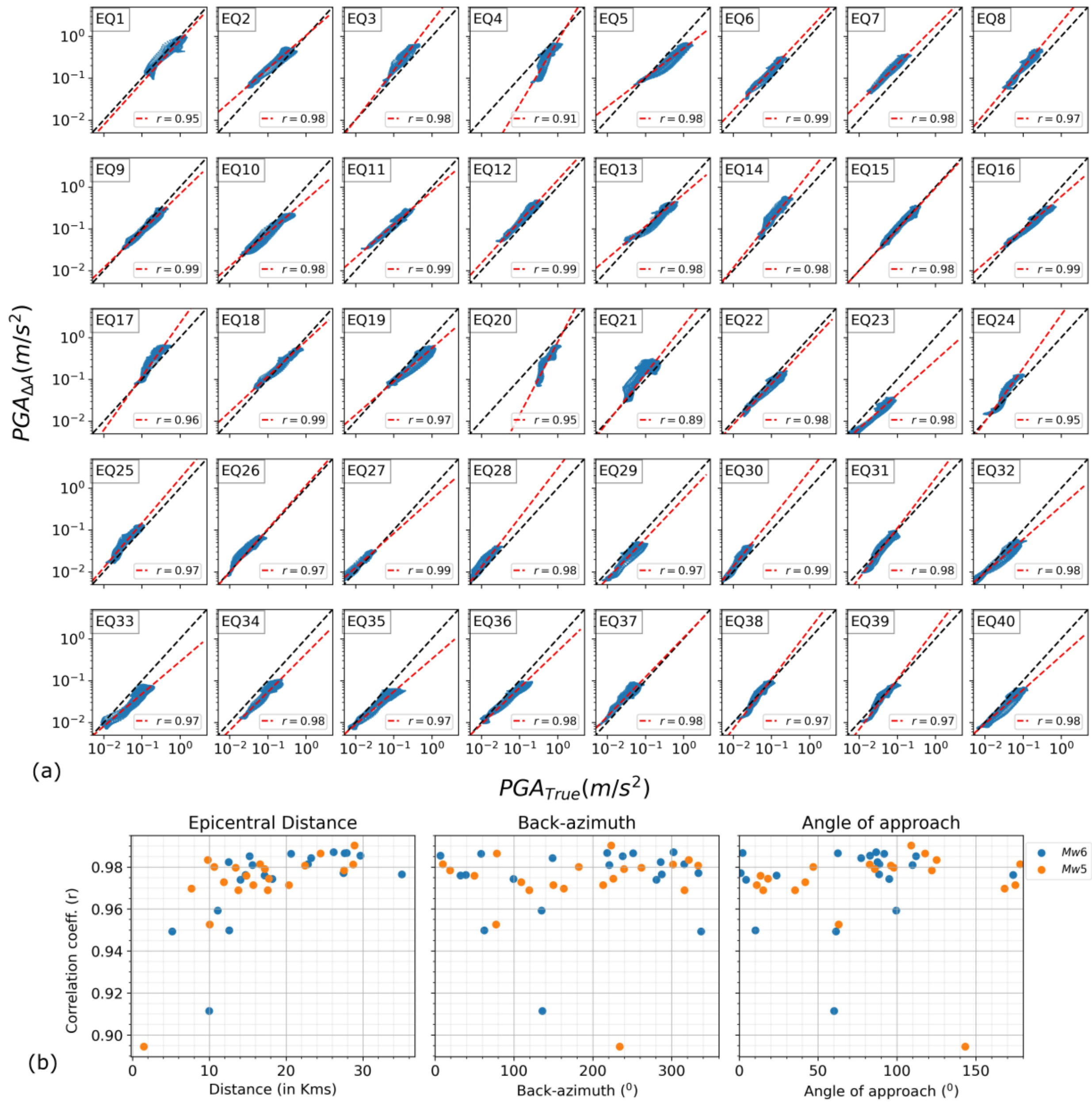

Figure 7: $\boldsymbol{PGA_{\Delta A}}$ *is calculated for all 40 earthquakes and compared with the simulated PGA values (*$\boldsymbol{PGA_{true}}$*). A) Shows the correlation between* $\boldsymbol{PGA_{\Delta A}}$ *and* $\boldsymbol{PGA_{true}}$ *for all earthquakes, where red dashed line shows the line of best fit and black dashes show the* $\boldsymbol{\gamma = 1}$ *line. The* $\boldsymbol{\gamma}$ *value is mentioned for all the earthquakes. B) Shows the* $\boldsymbol{\gamma}$ *value versus distribution of the following three parameters for all 40 earthquakes- epicentral distance, back-azimuth (bearing of line joining hypocenter to the center of Tomorrowville) and angle of approach (the azimuthal*

difference between the line connecting the hypocenter to the major fault asperity, and the line connecting the hypocenter to the center of Tomorrowville).

6 Discussion and summary

Estimates from UNDRR suggest that the number of people at risk from a major earthquake will increase from some 370 million in 2020 to more than 850 million by 2050 (UN-Habitat, 2022). Due to historically unprecedented rapid urbanization, these people will be increasingly concentrated in urban centers; the same source estimates that by 2050 global urban population will increase from the current 56% to around 68% with 95% of this growth happening in the global south. Without a concerted effort at providing decision support for high cost-benefit risk sensitive construction, ongoing urbanization in areas of high seismic hazard, will increase disaster risk for millions.

That the intensity of seismic shaking varies at high spatial frequencies is graphically demonstrated by large differences of seismic damage over very short distances in areas of uniform building code (Bielak et al., 1999; see also Asimaki et al., 2012; Dolce et al., 2003; Ohsumi et al., 2016; Sextos et al., 2018). What is less well known is the extent to which this variability is the result of differences in the earthquake source, or in contrasts in the rheological properties of the near surface that might impose a stable and estimable LF amplification, to first order independent of that source. The former prioritizes forecasting likely earthquake sources in seismic hazard assessment, while the latter suggests that measuring the properties of the near surface might produce a pathway to understanding spatial patterns of seismic shaking regardless of the source. This would in turn open a path to the development of physics-based, high-resolution building-code classification and support evidence based seismic urban planning policy.

Current methods for seismic hazard assessment require seismic catalogues built from long-term deployment of large numbers of seismometers to calibrate ground motion models (Douglas, 2017; Douglas & Aochi, 2008; Douglas & Edwards, 2016a). The observed variability around these models is assumed to be stochastic and statistical methods are used to provide the moments of the emerging distributions leading to low spatial resolution estimates of seismic hazard. Over most of the Global South such long-term data has not been collected nor is there any current appetite for deploying dense networks of seismometers required for this assessment at the resolution which would be required to guide seismic risk informed urban planning at actionable scales.

In this study we have harnessed the potential of high resolution PB earthquake simulations to explore the extent to which seismic intensity variability might be described by near-surface geology and that relative seismic intensity is independent of the earthquake source. Do some areas shake more than others, regardless of the earthquake? We exploit the certainty of a virtual world, Tomorrowville, in which the rheology, described by the geometry of the seismic velocity, is known everywhere, in which seismic sources are precisely described by kinematic models (Graves & Pitarka, 2010; Schmedes et al., 2013), and in which wave propagation is perfectly described by the wave propagation solver (SPEED) we use (Mazzieri et al., 2013)~~.~~~~In Tomorrowville, dense arrays of ideal seismometers record the wave field across the surface.~~ The choice of software should not lead to any notable deviation from the results obtained in this study. ~~In Tomorrowville, dense arrays of ideal seismometers record the wave field across the surface.~~

The study develops a Δ-***A*** decomposition, that splits the seismic process into a mean-field attenuation model, describing the amplitude decay with source-receiver distance, and an amplification field, describing the integrated amplification of the entire wave path as experienced at each point on the surface. We have shown methods for the estimation of the Δ model and for the ***A*** field for Tomorrowville and demonstrated that their description can be used estimate the true PGA field.

This study utilizes PB simulations in a virtual environment that shows a significant fraction of the observed variability can be explained without categorizing them as stochastic. In the real world, beyond these deterministic variations, stochastic elements of the process must be considered separately. Moreover, it becomes important to classify uncertainties as aleatory or epistemic, when the real data guides the model fitting and resulting deviations (Kiureghian & Ditlevsen, 2009). However, in this study, PB simulation results are assumed to be devoid of any modelling uncertainties (or aleatory variability) and they are treated as reproducible true solutions in the analysis. Consequently, the deviations obtained in the results of ~~figure~~Figure 7a~~A~~

are fundamentally epistemological. The difference between the amplification map for any event and the $\boldsymbol{A}$ field that determines the value of the local PGA, is precisely quantified and accessible. Investigations show that the maximum standard deviation of the $\boldsymbol{A}$ field is about 23.8% of the $\boldsymbol{lnA_j}$ measured across the entire area, that includes the source and path dependent variability. More importantly, analysis of the variability of the amplification value at any point, indicated stable convergence from as few as 7 event simulations. Furthermore, comparisons of amplifications at locations over the river basin with locations on basement in Tomorrowville, produced stable, order-of-magnitude differences in amplification which converged rapidly and which gave stable non-overlapping amplification estimates. Of course, both the stability and the contrast in amplification are functions of the choice of velocity distribution but the choice of model here was developed to reflect not uncommon velocity geometry not to accentuate amplification contrasts. We expect that the general conclusions of this work are independent of the details of the Tomorrowville velocity model.

We have not attempted to explore the variability of the amplification with the source parameters and the initial results suggest that the influence is not likely to be strong. The main candidates, source directivity and epicentral azimuth, expected to be dominant in the strongly anisotropic velocity model used here, do not make an appreciable systematic contribution to the $\boldsymbol{A}$~~$\boldsymbol{A_j}$~~ field. Descriptions of active fault geometry and seismotectonics of Tomorrowville could impose a source fabric introducing some systematic influence on the amplification field. Incorporation of any such influence could only constrain the variability so the results described here might be considered as a lower bound on the stability of the $\boldsymbol{A}$ field. The primary factor influencing ground motion amplification in this study is the basin geometry or buried topography, although the impact of surface topography is also anticipated to significantly affect the amplification pattern (García-Pérez et al., 2021; Geli et al., 1988; Lee et al., 2009; Poursartip et al., 2020). The surface topography, often rich in high-resolution data, is the most straightforward to control, and it is expected to contribute to the observed variability. Future research will concentrate on investigating the influence of surface topographic features, in addition to buried topography, on the amplification phenomenon.

The reconstruction of the simulated PGA fields provided further evidence of the efficacy of the method. Using estimates of the Δ and $\boldsymbol{A}$ components from a set of 39 simulations provided strong correlations between true and inverted PGA fields for the 40th. Further, in keeping with the observation of non-overlapping amplification values for basement and basin locations, places with high shaking were broadly consistently high for all events, locations experiencing low intensity shaking were also consistent across all events.

The results are suggestive of an underlying physical process in which small-scale LF *relative* shaking intensity is controlled more by local geology than by source process. Given the description of the relevant fields through simulations, each taking approximately a day on a commonly available computer clusters (see Table S3 for simulation parameters and run time estimates), it is feasible to estimate the entire PGA field ($PGA_{\Delta A}$) for an event of a specific magnitude and location in milliseconds of computing time.~~Thus, given the description of the relevant fields, it is possible in milliseconds of computing time, to estimate the entire PGA field for an event of a given magnitude and location which currently takes days of computation using commonly available computer clusters.~~ At the minimum, this provides a workflow through which normal probabilistic seismic hazard assessments, that require estimates of PGA for thousands of events at each location, can benefit from the advances in physics based simulations without the massive compute overhead that make these computations unfeasible at present.

The stability of the relative amplification field together with the stable, order of magnitude difference in PGA across the surface of Tomorrowville demonstrated in this study, points to methods for high-resolution seismic hazard estimation based on understanding the static properties of the near surface, rather than on the unpredictable properties of future earthquakes. The challenge becomes a problem of measurement, rather than forecasting. There remains the critical problem either of the elucidation of the velocity structure of the near surface (Sebastiano et al., 2019), so the Δ and $\boldsymbol{A}$ fields might be estimated through simulation as in this paper, or the direct estimation of the field by measurement of the intensity of shaking at high resolution in the area of interest. To clarify again, this study explores only LF near-surface effects arising from the presence of complex sedimentary basins and show their contribution in short-scale variability in amplification. It is~~'s~~ noteworthy that these LF effects are additional to the site effects related to very-near surface (decameter) depths, which include nonlinear soil responses and other high spatial-frequency velocity variations, all of which can lead to intricate outcomes (Taborda et al., 2012). Consequently, for applications like enhancing microzonation maps, it's imperative to merge this analysis with elements accounting for HF variability.

In conclusion, rapid urban expansion in areas of poor historical instrumentation leaves significant gaps in data for seismic hazard assessment. Furthermore, current methods both require decade long deployment of dense seismic networks in the area of near-future urban development and fail to provide high-resolution assessments that identify areas of strong and weak shaking that could underpin high cost-benefit seismic code classification. The potential of physics based simulations has prompted the evaluation of the seismic wave field across areas of near-future development. The results suggest methods to allow the rapid, high-resolution assessment of geological structure that could lead to risk assessment at unprecedented resolution. ~~Contemporary advances in ambient noise tomography techniques that are used for shallow crustal structure determination could make this a realistic approach (Bard et al., 2010).~~

Statements and Declarations

Acknowledgments

John McCloskey is listed as a co-author in recognition of his significant contributions. Unfortunately, he passed away after the manuscript was ready for submission, and we deeply mourn his loss.

Authors thank initial discussions and simulations obtained with the prompt support and guidance from Karim Tarbali, former PDRA at the University of Edinburgh. We thank Gemma Cremen, Chris J. Bean, Mark Naylor, Ian Main, Karen Lythgoe and two anonymous reviewers for providing constructive feedback and guidance in improving the manuscript.

Funding

This research is a part of the wider PhD project 'Physics-based Ground Motion Simulations and Uncertainity Assessment in Rapidly Urbanising Environments'. The PhD student is funded by University of Edinburgh, School of Geosciences. This research project is also supported by the Tomorrow Cities Hub (UKRI/GCRF fund under grant NE/S009000/1). ~~Authors thank initial discussions and simulations obtained with the prompt support and guidance from Karim Tarbali,~~

~~former PDRA at the University of Edinburgh. We thank Gemma Cremen, Chris J. Bean, Mark Naylor and Ian Main for providing constructive feedback and guidance in improving the manuscript.~~

Author Contributions

Both authors contributed to the study conception and design. Material preparation and data analysis were performed by HA. The first draft of the manuscript was prepared by HA including all the figures and text. The text was further reviewed and improved with the help of JM.

Rights Retention Statement

Open Research

The data used in this research are mainly the simulation outputs, which are extensive in scale. The ~~Consequently, we are actively involved in the process of archiving this data. Due to the substantial volume of this dataset, we aim to make it accessible through our institution's data-sharing platform, Edinburgh DATAshare (https://datashare.ed.ac.uk). It's important to note that~~ critical information regarding the crustal domain, earthquake hypocenter, and PGA data, which is pivotal for generating the majority of the manuscript's results, can be found in the supplementary material. For more detailed information on earthquake moment distribution, we encourage readers to refer to Jenkins et al. 2023. The software used to run the simulation is an open-source package, SPEED (Mazzieri et al., 2013). The data analysis and processing is done using ~~basic programming language,~~ Python and the code is available at https://github.com/himansh78/GroundMotionCalc.git.~~.~~

Competing Interests

The authors declare they have no conflict of interest.

References

Abrahamson, N. A., Silva, W. J., & Kamai, R. (2014). Summary of the ASK14 ground motion relation for active crustal regions. *Earthquake Spectra*, *30*(3), 1025–1055. https://doi.org/10.1193/070913EQS198M

Aki, K. (1993). Local site effects on weak and strong ground motion. *Tectonophysics*, *218*(1–3), 93–111. https://doi.org/10.1016/0040-1951(93)90262-I

Ancheta, T. D., Darragh, R. B., Stewart, J. P., Seyhan, E., Silva, W. J., Chiou, B. S. J., … Donahue, J. L. (2014). NGA-West2 database. *Earthquake Spectra*, *30*(3), 989–1005. https://doi.org/10.1193/070913EQS197M

Anderson, J. G., & Brune, J. N. (1999). Probabilistic Seismic Hazard Analysis without the Ergodic Assumption. *Seismological Research Letters*, *70*(1), 19–28. https://doi.org/10.1785/GSSRL.70.1.19

Ansal, A., Kurtuluş, A., & Tönük, G. (2010). Seismic microzonation and earthquake damage scenarios for urban areas. *Soil Dynamics and Earthquake Engineering*, *30*(11), 1319–1328. https://doi.org/10.1016/j.soildyn.2010.06.004

Asimaki, D., Ledezma, C., Montalva, G. A., Tassara, A., Mylonakis, G., & Boroschek, R. (2012). Site effects and damage patterns. *Earthquake Spectra*, *28*(S1), S55–S74. https://doi.org/10.1193/1.4000029

Asimaki, D., Mohammadi, K., Mason, H. B., Adams, R. K., Rajaure, S., & Khadka, D. (2017). Observations and Simulations of Basin Effects in the Kathmandu Valley during the 2015 Gorkha, Nepal, Earthquake Sequence: *Earthquake Spectra*, *33*(S1), S35–S53. https://doi.org/10.1193/013117EQS022M

Atkinson, G. M., & Boore, D. M. (2006). Earthquake Ground-Motion Prediction Equations for Eastern North America. *Bulletin of the Seismological Society of America*, *96*(6), 2181–2205. https://doi.org/10.1785/0120050245

Baker, J. W., Bradley, B. A., & Stafford, P. J. (2021). *Probabilistic seismic hazard and risk analysis*. Cambridge University Press.

Bazzurro, P., & Cornell, C. A. (2004). Nonlinear soil-site effects in probabilistic seismic-hazard analysis. *Bulletin of the Seismological Society of America*, *94*(6), 2110–2123. https://doi.org/10.1785/0120030216

Bielak, J., Xu, J., & Ghattas, O. (1999). Earthquake Ground Motion and Structural Response in Alluvial Valleys. *Journal of Geotechnical and Geoenvironmental Engineering*, *125*(5), 413–423. https://doi.org/https://doi.org/10.1061/(ASCE)1090-0241(1999)125:5(413)

Borcherdt, R. D., & Glassmoyer, G. (1992). On the characteristics of local geology and their influence on ground motions generated by the Loma Prieta earthquake in the San Francisco Bay region, California. *Bulletin of the Seismological Society of America*, *82*(2), 603–641. https://doi.org/10.1785/BSSA0820020603

Bradley, B. A. (2011). A framework for validation of seismic response analyses using seismometer array recordings. *Soil Dynamics and Earthquake Engineering*, *31*(3), 512–520. https://doi.org/10.1016/j.soildyn.2010.11.008

Bradley, B. A. (2015). Systematic ground motion observations in the Canterbury earthquakes and region-specific non-ergodic empirical ground motion modeling. *Earthquake Spectra*, *31*(3), 1735–1761. https://doi.org/https://doi.org/10.1193/053013EQS137M

Bradley, B. A. (2019). On-going challenges in physics-based ground motion prediction and insights from the 2010–2011 Canterbury and 2016 Kaikoura, New Zealand earthquakes. *Soil Dynamics and Earthquake Engineering*, *124*, 354–364. https://doi.org/10.1016/j.soildyn.2018.04.042

Brocher, T. M. (2005). Empirical Relations between Elastic Wavespeeds and Density in the Earth's Crust. *Bulletin of the Seismological Society of America*, *95*(6), 2081–2092. https://doi.org/10.1785/0120050077

Brocher, T. M. (2008). Compressional and shear-wave velocity versus depth relations for common rock types in northern California. *Bulletin of the Seismological Society of America*, *98*(2), 950–968. https://doi.org/10.1785/0120060403

Cadet, H., Macau, A., Benjumea, B., Bellmunt, F., & Figueras, S. (2011). From ambient noise recordings to site effect assessment: The case study of Barcelona microzonation. *Soil Dynamics and Earthquake Engineering*, *31*(3), 271–281. https://doi.org/10.1016/J.SOILDYN.2010.07.005

Campbell, K. W., & Bozorgnia, Y. (2014). NGA-West2 ground motion model for the average horizontal components of PGA, PGV, and 5% damped linear acceleration response spectra. *Earthquake Spectra*, *30*(3), 1087–1114. https://doi.org/10.1193/062913EQS175M

Castellaro, S., Mulargia, F., & Rossi, P. L. (2008). Vs30: Proxy for seismic amplification? *Seismological Research Letters*, *79*(4), 540–543. https://doi.org/10.1785/gssrl.79.4.540

Castellaro, S., & Musinu, G. (2023). Resonance versus Shape of Sedimentary Basins. *Bulletin of the Seismological Society of America*, *113*(2), 745–761. https://doi.org/10.1785/0120210277

Chiou, B. S. J., & Youngs, R. R. (2014). Update of the Chiou and Youngs NGA model for the average horizontal component of peak ground motion and response spectra. *Earthquake Spectra*, *30*(3), 1117–1153. https://doi.org/10.1193/072813EQS219M

Cramer, C. H. (2003). Site-specific seismic-hazard analysis that is completely probabilistic. *Bulletin of the Seismological Society of America*, *93*(4), 1841–1846. https://doi.org/10.1785/0120020206

Cremen, G., Galasso, C., McCloskey, J., Barcena, A., Creed, M., Filippi, M. E., … Trogrlić, R. Š. (2023). A state-of-the-art decision-support environment for risk-sensitive and pro-poor urban planning and design in Tomorrow's cities. *International Journal of Disaster Risk Reduction*, *85*, 103400. https://doi.org/10.1016/j.ijdrr.2022.103400

Day, S. M., Graves, R., Bielak, J., Dreger, D., Larsen, S., Olsen, K. B., … Ramirez-Guzman, L. (2019). Model for Basin Effects on Long-Period Response Spectra in Southern California: *Earthquake Spectra*, *24*(1), 257–277. https://doi.org/10.1193/1.2857545

De Hoop, A. T. (1958). Representation theorems for the displacement in an elastic solid and their application to elastodynamic diffraction theory . In *Technische Hogeschool, Delft, Netherland*. Technische Hogeschoo.

Dolce, M., Masi, A., Marino, M., & Vona, M. (2003). Earthquake damage scenarios of the building stock of Potenza (Southern Italy) including site effects. *Bulletin of Earthquake Engineering*, *1*(1), 115–140. https://doi.org/10.1023/A:1024809511362

Douglas, J. (2017). Ground motion prediction equations 1964-2019 (December 2019). *SED Report SED/ENSI/R/01/20140911*, *October*, 1–651. http://www.gmpe.org.uk/gmpereport2014.pdf

Douglas, J., & Aochi, H. (2008). A survey of techniques for predicting earthquake ground motions for engineering purposes. *Surveys in Geophysics*, *29*(3), 187–220. https://doi.org/10.1007/s10712-008-9046-y

Douglas, J., & Edwards, B. (2016a). Recent and future developments in earthquake ground motion estimation. *Earth-Science Reviews*, *160*, 203–219. https://doi.org/10.1016/j.earscirev.2016.07.005

Douglas, J., & Edwards, B. (2016b). Recent and future developments in earthquake ground motion estimation. In *Earth-Science Reviews* (Vol. 160, pp. 203–219). Elsevier B.V. https://doi.org/10.1016/j.earscirev.2016.07.005

Foti, S., Aimar, M., Ciancimino, A., & Passeri, F. (2019). Recent developments in seismic site response evaluation and microzonation. *Proceedings of the 17th European Conference on Soil Mechanics and Geotechnical Engineering, ECSMGE 2019*. https://doi.org/10.32075/17ECSMGE-2019-1117

Frankel, A. (1993). Three-dimensional simulations of ground motions in the San Bernardino Valley, California, for hypothetical earthquakes on the San Andreas Fault. *Bulletin of Seismological Society of America*, *83*(4), 1020–1041. https://doi.org/https://doi.org/10.1785/BSSA0830041020

Freddi, F., Galasso, C., Cremen, G., Dall'Asta, A., Di Sarno, L., Giaralis, A., … Woo, G. (2021). Innovations in earthquake risk reduction for resilience: Recent advances and challenges. *International Journal of Disaster Risk Reduction*, *60*. https://doi.org/10.1016/j.ijdrr.2021.102267

García-Pérez, T., Ferreira, A. M. G., Yáñez, G., Iturrieta, P., & Cembrano, J. (2021). Effects of topography and basins on seismic wave amplification: The Northern Chile coastal cliff and intramountainous basins. *Geophysical Journal International*, *227*(2), 1143–1167. https://doi.org/10.1093/gji/ggab259

Geli, L., Bard, P. Y., & Jullien, B. (1988). The effect of topography on earthquake ground motion: a review and new results. In *Bulletin - Seismological Society of America* (Vol. 78, Issue 1, pp. 42–63). https://doi.org/10.1016/0148-9062(88)90024-1

Gentile, R., Cremen, G., Galasso, C., Jenkins, L. T., Manandhar, V., Mentese, E. Y., … McCloskey, J. (2022). Scoring , selecting , and developing physical impact models for multi- hazard risk assessment. *International Journal of Disaster Risk Reduction*, *82*, 103365. https://doi.org/https://doi.org/10.1016/j.ijdrr.2022.103365

Graves, R. W., & Pitarka, A. (2010). Broadband ground-motion simulation using a hybrid approach. *Bulletin of the Seismological Society of America*, *100*(5 A), 2095–2123. https://doi.org/10.1785/0120100057

Graves, R. W., Pitarka, A., & Somerville, P. G. (1998). Ground-motion amplification in the Santa Monica area: Effects of shallow basin-edge structure. *Bulletin of the Seismological Society of America*, *88*(5), 1224–1242. https://doi.org/10.1785/bssa0880051224

Hough, S. E., & Anderson, J. G. (1988). High-frequency Spectra Observed at Anza, California: Implications for Q Structure. *Bulletin of the Seismological Society of America*, *78*(2), 692–707. https://doi.org/https://doi.org/10.1785/BSSA0780020692

Hough, S. E., Martin, S. S., Gahalaut, V., Joshi, A., Landes, M., & Bossu, R. (2016). A comparison of observed and predicted ground motions from the 2015 MW7.8 Gorkha, Nepal, earthquake. *Natural Hazards*, *84*(3), 1661–1684. https://doi.org/https://doi.org/10.1007/s11069-016-2505-8

Jenkins, L. T., Creed, M. J., Tarbali, K., Muthusamy, M., Trogrlić, R. Š., Phillips, J. C., … McCloskey, J. (2023). Physics-based simulations of multiple natural hazards for risk-sensitive planning and decision-making in expanding urban regions. *International Journal* *of Disaster Risk Reduction*, *84*, 103338. https://doi.org/https://doi.org/10.1016/j.ijdrr.2022.103338

Kaklamanos, J., Bradley, B. A., Thompson, E. M., & Baise, L. G. (2013). Critical parameters affecting bias and variability in site-response analyses using KiK-net downhole array data. *Bulletin of the Seismological Society of America*, *103*(3), 1733–1749. https://doi.org/10.1785/0120120166

Kamai, R., Abrahamson, N. A., & Silva, W. J. (2016). VS30 in the NGA GMPEs: Regional differences and suggested practice. *Earthquake Spectra*, *32*(4), 2083–2108. https://doi.org/10.1193/072615EQS121M

Kiureghian, A. Der, & Ditlevsen, O. (2009). Aleatory or epistemic? Does it matter? *Structural Safety*, *31*(2), 105–112. https://doi.org/10.1016/j.strusafe.2008.06.020

Knopoff, L. (1956). Diffraction of Elastic Waves. *The Journal of the Acoustical Society of America*, *28*, 217. https://doi.org/10.1121/1.1908247

Kramer, S. L. (1996). *Geotechnical Earthquake Engineering*. Pearson Prentice-Hall, Upper Saddle River, NJ, USA.

Kramer, S. L., & Mitchell, R. A. (2006). Ground Motion Intensity Measures for Liquefaction Hazard Evaluation: *Earthquake Spectra*, *22*(2), 413–438. https://doi.org/10.1193/1.2194970

Kuehn, N. M., Abrahamson, N. A., & Walling, M. A. (2019). Incorporating Nonergodic Path Effects into the NGA-West2 Ground-Motion Prediction Equations. *Bulletin of the Seismological Society of America Seismological Society of America*, *109*(2), 575–585. https://doi.org/10.1785/0120180260

Landwehr, N., Kuehn, N. M., Scheffer, T., & Abrahamson, N. (2016). A Nonergodic Ground-Motion Model for California with Spatially Varying Coefficients. *Bulletin of the Seismological Society of America*, *6*, 2574–2583. https://doi.org/10.1785/0120160118

Lee, S. J., Komatitsch, D., Huang, B. S., & Tromp, J. (2009). Effects of topography on seismic-wave propagation: An example from Northern Taiwan. *Bulletin of the Seismological Society* *of America*, *99*(1), 314–325. https://doi.org/10.1785/0120080020

Liu, P., Archuleta, R. J., & Hartzell, S. H. (2006). *Prediction of Broadband Ground-Motion Time Histories : Hybrid Low / High- Frequency Method with Correlated Random Source Parameters*. *96*(6), 2118–2130. https://doi.org/10.1785/0120060036

Marafi, N. A., Eberhard, M. O., Berman, J. W., Wirth, E. A., & Frankel, A. D. (2017). Effects of deep basins on structural collapse during large subduction earthquakes. *Earthquake Spectra*, *33*(3), 963–997. https://doi.org/10.1193/071916EQS114M

Maufroy, E., Cruz-Atienza, V. M., & Gaffet, S. (2012). A robust method for assessing 3-D topographic site effects: A case study at the LSBB underground laboratory, France. *Earthquake Spectra*, *28*(3), 1097–1115. https://doi.org/10.1193/1.4000050

Mazzieri, I., Stupazzini, M., Guidotti, R., & Smerzini, C. (2013). SPEED: SPectral Elements in Elastodynamics with Discontinuous Galerkin: a non-conforming approach for 3D multi-scale problems. *International Journal for Numerical Methods in Engineering*, *95*(12), 991–1010. https://doi.org/10.1002/NME.4532

Mazzieri, I., Stupazzini, M., Guidotti, R., Smerzini, C., Mazzieri, I., Stupazzini, M., … Smerzini, C. (2013). SPEED: SPectral Elements in Elastodynamics with Discontinuous Galerkin: a non-conforming approach for 3D multi-scale problems. *IJNME*, *95*(12), 991–1010. https://doi.org/10.1002/NME.4532

Mcguire, R. K. (2008). Probabilistic seismic hazard analysis: Early history. *Earthquake Engineering & Structural Dynamics*, *37*, 329–338. https://doi.org/10.1002/eqe.765

Menteşe, E. Y., Cremen, G., Gentile, R., Galasso, C., Filippi, E. M., & McCloskey, J. (2023). Future exposure modelling for risk-informed decision making in urban planning. *International Journal of Disaster Risk Reduction*, *90*, 103651. https://doi.org/10.1016/j.ijdrr.2023.103651

Mucciarelli, M., & Gallipoli, M. R. (2006). Comparison between Vs30 and other estimates of site amplification in Italy. *First European Conference on Earthquake Engineering and Seismology*, *September*, 270.

Nath, S. K., & Thingbaijam, K. K. S. (2011). Peak ground motion predictions in India: an appraisal for rock sites. *Journal of Seismology*, *15*(2), 295–315. https://doi.org/https://doi.org/10.1007/s10950-010-9224-5

Ohsumi, T., Mukai, Y., & Fujitani, H. (2016). Investigation of Damage in and Around Kathmandu Valley Related to the 2015 Gorkha, Nepal Earthquake and Beyond. *Geotechnical and Geological Engineering*, *34*(4), 1223–1245. https://doi.org/10.1007/s10706-016-0023-9

Oral, E., Ayoubi, P., Ampuero, J. P., Asimaki, D., & Bonilla, L. F. (2022). Kathmandu Basin as a local modulator of seismic waves: 2-D modelling of non-linear site response under obliquely incident waves. *Geophysical Journal International*, *231*(3), 1996–2008. https://doi.org/10.1093/gji/ggac302

Paolucci, R., Mazzieri, I., Smerzini, C., & Stupazzini, M. (2014). Physics-Based Earthquake Ground Shaking Scenarios in Large Urban Areas. *Geotechnical, Geological and Earthquake Engineering*, *34*, 331–359. https://doi.org/10.1007/978-3-319-07118-3_10

Pilz, M., Parolai, S., Stupazzini, M., Paolucci, R., & Zschau, J. (2011). Modelling basin effects on earthquake ground motion in the Santiago de Chile basin by a spectral element code. *Geophys. J. Int*, *187*, 929–945. https://doi.org/10.1111/j.1365-246X.2011.05183.x

Pitilakis, K., Riga, E., Anastasiadis, A., Fotopoulou, S., & Karafagka, S. (2019). Towards the revision of EC8: Proposal for an alternative site classification scheme and associated intensity dependent spectral amplification factors. *Soil Dynamics and Earthquake Engineering*, *126*, 105137. https://doi.org/https://doi.org/10.1016/j.soildyn.2018.03.030

Poursartip, B., Fathi, A., & Tassoulas, J. L. (2020). Large-scale simulation of seismic wave motion: A review. *Soil Dynamics and Earthquake Engineering*, *129*, 105909. https://doi.org/10.1016/j.soildyn.2019.105909

Rodriguez-Marek, A., Rathje, E. M., Bommer, J. J., Scherbaum, F., & Stafford, P. J. (2014). Application of Single-Station Sigma and Site-Response Characterization in a Probabilistic Seismic-Hazard Analysis for a New Nuclear Site. *Bulletin of Seismological Society of*

America, *104*(4), 1601–1619. https://doi.org/10.1785/0120130196

Schmedes, J., Archuleta, R. J., & LavalÍee, D. (2013). A kinematic rupture model generator incorporating spatial interdependency of earthquake source parameters. *Geophysical Journal International*, *192*(3), 1116–1131. https://doi.org/10.1093/gji/ggs021

Sebastiano, D., Francesco, P., Salvatore, M., Roberto, I., Antonella, P., Giuseppe, L., … Daniela, F. (2019). Ambient noise techniques to study near-surface in particular geological conditions: A brief review. In *Innovation in Near-Surface Geophysics: Instrumentation, Application, and Data Processing Methods* (pp. 419–460). Elsevier Inc. https://doi.org/10.1016/B978-0-12-812429-1.00012-X

Semblat, J. F., Kham, M., Parara, E., Bard, P. Y., Pitilakis, K., Makra, K., & Raptakis, D. (2005). Seismic wave amplification: Basin geometry vs soil layering. *Soil Dynamics and Earthquake Engineering*, *25*(7–10), 529–538. https://doi.org/10.1016/j.soildyn.2004.11.003

Sextos, A., De Risi, R., Pagliaroli, A., Foti, S., Passeri, F., Ausilio, E., … Zimmaro, P. (2018). Local site effects and incremental damage of buildings during the 2016 Central Italy Earthquake sequence. *Earthquake Spectra*, *34*(4), 1639–1669. https://doi.org/10.1193/100317EQS194M

Shi, J., & Asimaki, D. (2017). From Stiffness to Strength: Formulation and Validation of a Hybrid Hyperbolic Nonlinear Soil Model for Site-Response Analyses. *Bulletin of the Seismological Society of America*, *107*(3), 1336–1355. https://doi.org/10.1785/0120150287

Smerzini, C., Paolucci, R., & Stupazzini, M. (2011). Comparison of 3D, 2D and 1D numerical approaches to predict long period earthquake ground motion in the Gubbio plain, Central Italy. *Bulletin of Earthquake Engineering*, *9*(6), 2007–2029. https://doi.org/10.1007/s10518-011-9289-8

Smerzini, C., & Villani, M. (2012). Broadband numerical simulations in complex near-field geological configurations: The case of the 2009 Mw 6.3 L'Aquila earthquake. *Bulletin of the Seismological Society of America*, *102*(6), 2436–2451. https://doi.org/10.1785/0120120002

Spudich, P., Bayless, J. R., Baker, J., Chiou, B. S. J., Rowshandel, B., Shahi, S., & Somerville, P. (2013). Final Report of the NGA-West2 Directivity Working Group. In *Pacific Engineering Research Center Report* (Issue 09).

Stewart, J. P., Afshari, K., & Goulet, C. A. (2017). Non-ergodic site response in seismic hazard analysis. *Earthquake Spectra*, *33*(4), 1385–1414. https://doi.org/10.1193/081716EQS135M

Stirling, M. W. (2014). The Continued Utility of Probabilistic Seismic-Hazard Assessment. In *Earthquake Hazard, Risk and Disasters* (pp. 359–376). Elsevier Inc. https://doi.org/10.1016/B978-0-12-394848-9.00013-4

Stirling, M. W., McVerry, G., Gerstenberger, M., Litchfield, N., Van Dissen, R., Berryman, K., … Jacobs, K. (2012). National seismic hazard model for New Zealand: 2010 update. *Bulletin of the Seismological Society of America*, *102*(4), 1514–1542. https://doi.org/10.1785/0120110170

Taborda, R., Bielak, J., & Restrepo, D. (2012). Earthquake Ground-Motion Simulation including Nonlinear Soil Effects under Idealized Conditions with Application to Two Case Studies. *Seismological Research Letters*, *83*(6), 1047–1060. https://doi.org/10.1785/0220120079

Taborda, R., Roten, D., & Diego, S. (2014). Physics-Based Ground-Motion Simulation. In *Encyclopedia of Earthquake Engineering* (Issue January, pp. 1–33). https://doi.org/10.1007/978-3-642-36197-5

Torre, C. A. de la, Bradley, B. A., & Lee, R. L. (2020). Modeling nonlinear site effects in physics-based ground motion simulations of the 2010–2011 Canterbury earthquake sequence: *Earthquake Spectra*, *36*(2), 856–879. https://doi.org/10.1177/8755293019891729

Tsai, C. C., Kishida, T., & Lin, W. C. (2021). Adjustment of site factors for basin effects from site response analysis and deep downhole array measurements in Taipei. *Engineering Geology*, *285*(June 2020), 106071. https://doi.org/10.1016/j.enggeo.2021.106071

UN-Habitat. (2022). World Cities Report 2020: Envisaging the Future of Cities. In *World Cities Report 2020: Envisaging the Future of Cities*. UN.

UNISDR, U. (2015). Sendai framework for disaster risk reduction 2015-2030. *Proceedings of the 3rd United Nations World Conference on DRR*.

Wang, C., Cremen, G., Gentile, R., & Galasso, C. (2023). Design and assessment of pro-poor financial soft policies for expanding cities. *International Journal of Disaster Risk Reduction*, *85*(December 2022), 103500. https://doi.org/10.1016/j.ijdrr.2022.103500

Wang, G., Du, C., Huang, D., Jin, F., Koo, R. C. H., & Kwan, J. S. H. (2018). Parametric models for 3D topographic amplification of ground motions considering subsurface soils. *Soil Dynamics and Earthquake Engineering*, *115*(September 2017), 41–54. https://doi.org/10.1016/j.soildyn.2018.07.018

Wells, D. L., & Coppersmith, K. J. (1994). New empirical relationships among magnitude, rupture length, rupture width, rupture area, and surface displacement. *Bulletin - Seismological Society of America*, *84*(4), 974–1002. https://doi.org/10.1785/bssa0840040974

Yomogida, K., & Etgen, J. T. (1993). 3-D wave propagation in the Los Angeles Basin for the Whittier-Narrows earthquake. *Bulletin of the Seismological Society of America*, *83*(5), 1325–1344. https://doi.org/10.1086/622062

Zhu, C., Thambiratnam, D., & Gallage, C. (2018). Statistical analysis of the additional amplification in deep basins relative to the 1D approach. *Soil Dynamics and Earthquake Engineering*, *104*, 296–306. https://doi.org/10.1016/j.soildyn.2017.09.003